Master's thesis
Materials physics

Fracture mechanical and mechanical characterisation of Alloy 52 dissimilar metal welds

Pentti Arffman

15.04.2019

Supervisors: Sebastian Lindqvist
prof. Simo Huotari

Examiners: prof. Kim Wallin
prof. Simo Huotari

University of Helsinki
Faculty of Science

PL 64 (Gustaf Hällströmin katu 2a)
00014 Helsingin yliopisto

HELSINGIN YLIOPISTO
HELSINGFORS UNIVERSITET
UNIVERSITY OF HELSINKI
MATEMAATTIS-LUONNONTIETEELLINEN TIEDEKUNTA
MATEMATISK-NATURVETENSKAPLIGA FAKULTETEN
FACULTY OF SCIENCE

Tiedekunta – Fakultet – Faculty	Koulutusohjelma – Utbildningsprogram – Degree programme
Mat-lu	Fysiikka

Tekijä – Författare – Author
Arffman Pentti Henrik Elias

Työn nimi – Arbetets titel – Title
Fracture mechanical and mechanical characterisation of Alloy 52 dissimilar metal welds

Työn laji – Arbetets art – Level	Aika – Datum – Month and year	Sivumäärä – Sidoantal – Number of pages
Pro gradu	15.4.2019	60

Tiivistelmä – Referat – Abstract

Dissimilar metal welds(DMW) in nuclear power plants have been identified to be prone to failure by cracking. Generally cracks grow straight, unless a weaker microstructure is adjacent. In DMWs cracks have propagated to the fusion line. Fracture toughness of weldments has been reported to sink in the same location.

It has been shown that hardness can be used to predict strength of a homogeneous material. In this thesis, such model was applied to DMWs. On the other hand, fracture toughness and crack propagation was studied for both ductile and brittle specimens.

Two DMWs were studied, MU1 and NI1. They shared the same SS base metal and Alloy 52 weld metal. Furthermore the LAS base metals were very similar: 18MND5 and SA508 for MU1 and NI1, respectively. NI1 specimens were studied in three different ageing conditions. Some of the data was reutilized from previous projects.

Vickers hardness was measured over the LAS fusion line. To be able to utilize hardness measurements without knowledge of their distribution, the data was bootstrapped. The means of the bootstrapped medians provided estimates of the average hardness and its deviation.

Three tensile specimens were tested from four different locations. Tensile results were compared to strength predictions from hardness. The VTT model developed for homogeneous materials predicted strength from hardness inadequately in its original form. However, once the parameters were varied, predictions agreed with measurements.

Ductile specimens were made from both MU1 and NI1. Temperatures for testing were 300°C and 20°C for MU1 and NI1 respectively. Their fracture toughness was determined with JIc, which is defined in ASTM E1820. Crack path was studied with either cross-cutting or profilometry. In the case of profilometry, the specimens were profiled from three different locations and the mean of results was used.

Brittle specimens were all from NI1. ASTM E1921 determines cleavage fracture toughness Jc. Test temperatures were between −80°C and −130°C. Crack path was studied with profilometry. Profiling location was at cleavage nucleation point. The point was determined with scanning electron microscope. The accuracy of profilometry itself was confirmed by comparing the results to specimen cross-cuts.

Linear correlation between fracture toughnesses and crack jumps towards fusion line was established successfully for most datasets. Ageing of the specimens reduced the fracture toughness of brittle specimens, but not of ductile ones. Instead, ductile fracture toughness increased with test temperature.

Avainsanat – Nyckelord – Keywords
Dissimilar metal welds, crack propagation, fracture toughness, hardness, strength

Säilytyspaikka – Förvaringställe – Where deposited
ethesis.helsinki.fi

Muita tietoja – Övriga uppgifter – Additional information

CONTENTS

Glossary viii

Acknowledgements x

1 INTRODUCTION 1

2 FRACTURE MECHANICS AND MATERIAL DEFORMATION 3

2.1 Strength . . . 5

2.2 Hardness . . . 5

2.3 Correlation between hardness and strength . . . 6

2.4 J-integral . . . 8

2.5 Tearing resistance curve . . . 10

2.6 Fracture mechanisms and crack propagation . . . 11

2.6.1 Brittle fracture . . . 11

2.6.2 Ductile fracture . . . 12

2.6.3 Impact of temperature on fracture mechanism and fracture toughness . . . 13

3 DISSIMILAR METAL WELDS 15

3.1 Microstructure . . . 15

3.2 Stress and strain behaviour . . . 17

3.3 Crack propagation around to the LAS-WM fusion line . . . 18

4 METHODOLOGY 19

4.1 Data collection and digitization . . . 19

4.2 Hardness testing . . . 19

4.3 Fracture toughness testing . . . 20

4.3.1 Specimen configurations . . . 21

4.3.2 Ductile fracture toughness . . . 22

4.3.3 Brittle fracture toughness . . . 24

4.4 Crack path profiling . . . 25

4.5 Scanning electron microscopy . . . 26

5 MEASUREMENTS 27

5.1 Test materials and specimens . . . 27

5.2 Hardness and strength of NG-DMWs . . . 28

5.3 Crack path and ductile fracture toughness 28
5.4 Crack path and brittle fracture toughness 29
6 RESULTS AND DISCUSSION 34
6.1 Hardness of an Alloy 52 DMW 34
6.2 Hardness and strength correlation for an Alloy 52 DMW 35
6.3 Crack path and ductile fracture of an Alloy 52 DMW 38
6.4 Crack path and J_C for an Alloy 52 DMW 41
7 CONCLUSION 44

LIST OF FIGURES

Figure 1 Schematic comparison of typical engineering and true stress-strain curves. 4
Figure 2 VTT model for hardness and strength correlation. 7
Figure 3 Stress-strain behaviours of nonlinear elastic and elastic-plastic materials during a loading-unloading cycle. 8
Figure 4 Visualization of the arbitrary path of J-integral around the crack tip. 9
Figure 5 Illustration of fracture toughness definitions utilized. 10
Figure 6 Schematic illustration of different tearing resistance curves. . 11
Figure 7 An illustration of ductile crack growth. 12
Figure 8 Schemation presentation of the different regions around a LAS-WM fusion line. 16
Figure 9 An example of digitized data from an OM fractograph. 20
Figure 10 Principle of calculating J. 21
Figure 11 Different specimen configurations. 21
Figure 12 The principle of elastic compliance method. 23
Figure 13 Typical tearing resistance curve for a ductile metallic material. 24
Figure 14 Illustrations of profiling paths for brittle and ductile specimens. 29
Figure 15 An example of a ductile crack profile. 30
Figure 16 One of the SEM fractographs of a brittle crack front. 30
Figure 17 An example of a brittle crack profile. 32
Figure 18 A magnification of verification around the crack tip. 32
Figure 18 Error estimation of brittle fracture crack propagation. 33
Figure 19 Results of hardness testing of MU1 DMW on the LAS border. 35
Figure 20 VTT model for LAS side with results from tests. 36
Figure 21 VTT model for hardness and strength applied to minimum hardness data. 37
Figure 22 VTT model for hardness and strength applied to median hardness data. 37

Figure 23 Tearing resistance curves and distances to fusion line for MU1 10x10. 38
Figure 24 Tearing resistance curves and distances to fusion line for MU1 10x20. 39
Figure 25 Ductile fracture toughness compared to maximum crack jump during the first 1mm of crack extension. 40
Figure 26 Cross-cuts of two MULTIMETAL 10x20 SE(B) specimens. . . . 41
Figure 27 J_c values compared to measured jumps towards fusion line while grouped according to ageing condition. 42
Figure 28 J_c values compared to measured jumps towards fusion line, divided by color into testing temperature groups. 43

LIST OF TABLES

Table 1 Test matrix for measured specimens. 27
Table 2 Chemical composition of mock-up materials. 28

GLOSSARY

Δ Crack extension. 23, 38

α Parameter for Ramberg-Osgood model of stress-strain curve. 4

ϵ Engineering strain. 3, 4

ϵ_T True strain. 3

σ Engineering stress. 3, 4

σ_{TS} Tensile strength. 5, 28

σ_T True stress. 3

σ_y Flow strength. 5, 7, 23

σ_{YS} Yield stress. 4, 5, 7, 28

A_0 Initial cross-sectional area of the specimen. 3

A_i Instantaneous cross-sectional area of the specimen. 3

ASTM American Society for Testing and Materials. 19–22, 24, 28

C(T) Compact tension specimen. 21, 22, 44

d Distance to fusion line. 29, 31, 34, 38, 40–42, 44–46

DBTT Ductile-brittle transition temperature. 13

DMW Dissimilar metal weld. 1, 2, 11, 15–18, 27, 34–36, 40, 44, 46

E Elastic modulus. 4, 25, 36

F Force applied to test specimen. 3

FL Fusion line. 1, 2, 16–18, 34, 39, 44, 45

FZ Fusion zone. 15

g Standard gravity. 7

HV Vickers hardness. 7, 19

HAZ Heat-affected zone. 1, 16–18, 34, 39, 44, 45

J J-integral, measure of fracture toughness. 8–10, 20, 21, 23, 38

J_c Elastic-plastic fracture toughness at the onset of cleavage fracture. 10, 20, 24, 25, 27, 41–43, 45

J_{Ic} Elastic-plastic fracture toughness under crack-tip plane-strain conditions at the onset of ductile fracture. 10, 14, 20, 22–24, 27, 28, 39–41, 44, 45

l_0 Initial length of a tensile specimen. 3

l_i Instantaneous length of a tensile specimen. 3

LAS Low-alloy steel. 15–18, 28, 34–36, 39, 40, 44

M' Point corresponding with M on true stress-strain curve. 3, 4

M Point of maximum stress on engineering stress-strain curve. ix, 3–5

M Strength mismatch factor. 28

n Strain hardening exponent. 4, 7

OM optical microscope. 19, 20, 25–27, 31

P_{nuc} Nucleation point of brittle fracture. 29

P Proportional limit. 3, 5

PMZ Partially melted zone. 16

PWHT Post-weld heat treatment. 1, 28

SE(B) Single-edge notched bend specimen. 21, 22, 38–41, 44

SEM scanning electron microscope. 26, 27, 30–32

SS Stainless steel. 28

WM Weld metal. 15–18, 34, 35

ACKNOWLEDGEMENTS

This paper is written at VTT Technical Research Centre of Finland as a Master's thesis to the Department of Physics at the University of Helsinki.

I would like to thank my supervisor at VTT, Sebastian Lindqvist, for advising me throughout the work. His contribution has been invaluable. On the other hand, Päivi Karjalainen-Roikonen has to be mentioned for having faith in me to give me such an assignment. Furthermore, Hanna Iitti, Jari Lydman and Marketta Mattila assisted me by conducting and instructing me in measurements. In the other end, my supervisor at University of Helsinki, professor Simo Huotari, assisted me in transforming my work into a thesis. Without these people, there would be nothing.

My studies have taken quite a long time. I have to thank all the people around me that have supported me. Especially my family have had unwavering faith in my ability. Thank you, everyone that has lifted me up when I was feeling down.

Espoo, 18.3.2019

Pentti Arffman

1 INTRODUCTION

Welding is used extensively to join metal objects together. The joined object resulting from welding is microstructurally different from the original objects as the material around the weld is melted and solidified. Consequently, the fracture resistance of a welded joint is also different from unwelded material. These discrepancies are even more pronounced when different metals are welded together, creating dissimilar metal welds (DMW).

DMW joints are needed in reactor pressure vessels of nuclear power plants to join together the ferritic vessel body and austenitic pipelines. Several cracks have been reported in these joints since an incident at the V.C. Summer power plant in 2000[1]. This has raised concern about the integrity of DMWs.

The surveillance materials are very limited and expensive. In addition, material strength can change dramatically over small distances. Nondestructive and spatially precise testing methods are therefore highly sought. One such method could be hardness testing, if hardness could be utilized to predict strength.

Not only the melted material is affected by welding. The heat from the weld pool also warms the adjacent material close to melting temperature. This region forms the heat-affected zone (HAZ). Heating and cooling of the HAZ change the microstructure, which affect the material properties such as hardness, strength and fracture toughness. In addition, mismatch in the joined materials enables the development of residual stresses on the fusion line (FL) during cooling. Post-weld heat treatment (PWHT) to relieve these stresses further alters the microstructure due to element migration and other consequences.

All of the effects above contribute to a complex state, where fracture toughness is lower around the fusion line than in the surrounding material. In general, a crack propagates straight unless a weaker microstructural zone is close or the crack is located in an region with strength mismatch. A strength mismatch in the joined materials causes a crack to grow towards the region with lower strength. Cracks originating in the HAZ have been recorded to deviate out-of-plane to the FL [2], something that is unheard of in regular, macroscopically homogeneous steels.

From a fracture mechanical standpoint, limited understanding means poor predictability. As the cracks normally grow straight, the fracture toughness affiliated with a slanted crack is not trivial. If a correlation between the slanted crack path and measured fracture toughness could be established, criticality of existing cracks could be predicted.

In this thesis, a few separate but interconnected questions are studied. The correlation between hardness and strength is studied by applying an existing model for homogeneous materials to hardness data measured over the FL of a DMW. To investigate the correlation between the slanted crack and fracture toughness, existing fracture toughness data was reutilized by reexamining the specimens with profilometry and scanning electron microscopy. Two different measures of fracture toughness are applied, one for brittle(cleavage) and another for ductile fracture.

The different questions are connected by the material: they are all studied around weldments, Alloy 52 DMWs to be precise. To sum up, the problems studied can be expressed in two questions. First, can the strength of an Alloy 52 DMW be predicted from its hardness? Second, how is the fracture resistance of an Alloy 52 DMW dependent on the distance of the initial crack to the FL? Answering these questions can potentially increase the safety and decrease the maintenance need of power plants.

2 FRACTURE MECHANICS AND MATERIAL DEFORMATION

Fracture mechanical and mechanical properties of materials are generally tested by controlled deformation of specimens. In tensile testing for example, test specimens are subjected to increasing tension, causing them to stretch and eventually break. Meanwhile elongation and load induced are measured. This produces stress-strain curves, which form the basis for further analysis.

Stress σ and strain ϵ are given by their engineering definition,

$$\sigma = \frac{F}{A_0}, \qquad (1) \qquad\qquad \epsilon = \frac{l_i - l_0}{l_0} = \frac{\Delta l}{l_0}, \qquad (2)$$

where F is the applied force and A_0 is the initial cross-sectional area normal to the applied force. l_i and l_0 are the current and initial length of the specimen, respectively. [3, pp. 114–116]

Sometimes it is better to use true stress and strain, which are defined by the instantaneous state of the specimen, that is

$$\sigma_T = \frac{F}{A_i}, \qquad (3) \qquad\qquad \epsilon_T = \ln \frac{l_i}{l_0}, \qquad (4)$$

where A_i is the current cross-sectional area.

Engineering and true stress-strain curves are illustrated in figure 1. As long as the applied stress stays within the elastic limits, that is before the proportional limit point P, the curves are similar. Once the stress starts to cause plastic deformation, the material starts to exhibit strain hardening and is able to withstand ever larger stresses. However, the reduction in cross-sectional area causes a reduction in the total load-bearing capacity of the specimen. While the true curve recognizes this, engineering does not and the two curves start to deviate from one another. Engineering and true values are related:

$$\sigma_T = \sigma(1 + \epsilon), \qquad (5) \qquad\qquad \epsilon_T = \ln(1 + \epsilon). \qquad (6)$$

The difference is evident from points M and M′, which correspond with each other on their respective curves. [3, pp. 131–132]

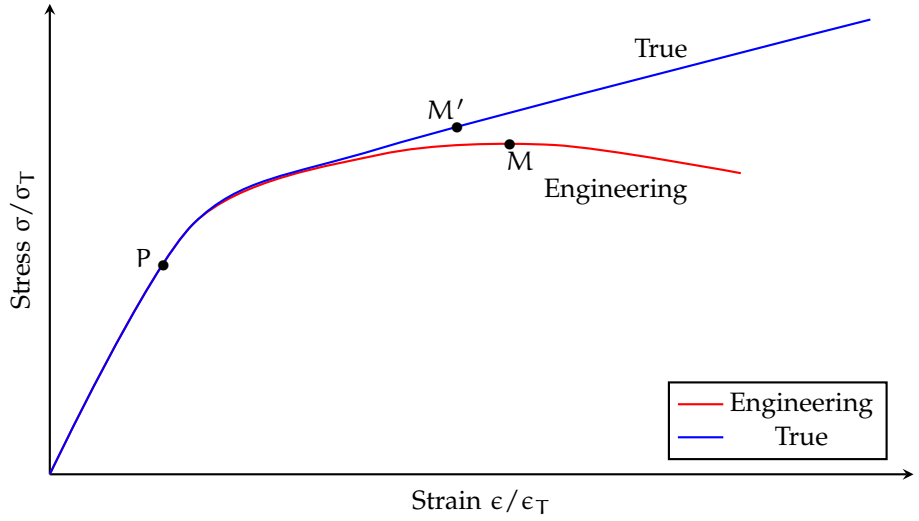

Figure 1: Schematic comparison of typical engineering and true stress-strain curves. Adapted from Callister [3, p. 132]

In fact, engineering and true values are related to each other only until M and M′. From that point forward necking occurs. Necking refers to a phenomenon where the specimen starts to thin out dramatically from one section leaving others unaltered. This section will ultimately be the point of fracture.

While true stress and strain gives a more realistic picture of the material's properties, the need for real-time measurement of the cross-sectional area makes them much more challenging to record. Also, majority of developed material parameters are designed to deploy the engineering curve.

For nonlinear curve-fitting of stress-strain data, the most widely used model is the Ramberg-Osgood equation and different applications of it. In this model,

$$\epsilon = \frac{\sigma}{E} + \alpha\frac{\sigma}{E}\left(\frac{\sigma}{\sigma_{YS}}\right)^{n-1}, \tag{7}$$

where E is the elastic modulus and α, n are fitting parameters. n is commonly known as strain-hardening exponent. α is a dimensionless constant which can be approximated from (offset) yield strength so that

$$n = \epsilon_{off}\frac{E}{\sigma_{YS}}, \tag{8}$$

where ϵ_{off} is the yield offset as discussed in the next section. [4]

While stress and strain are well defined, they are not always applicable. The stress state of a specimen under uniaxial tension is elementary. In more complex

situations such as fracture mechanical testing, a tensor representation of the stress field would be required. Measurement of such stress fields is extremely difficult if not impossible. In these cases, load P and displacement Δ are utilized.

2.1 STRENGTH

Strength refers to certain engineering stresses the material is able to bear. It is employed to distinguish strength as material property and stress as a measured quantity related to the applied load.

A typical engineering stress-strain curve for an elastic-plastic metallic material is illustrated in figure 1. The material experiences a gradual transition from elastic to plastic once the curve begins to deviate from the initial linear slope after P.

The maximum stress the material can withstand without irreversible deformation is naturally a point of interest. The stress at this point is called yield strength σ_{YS}. The location of P is ambiguous as it depends on the accepted deviation from linearity. Also, complete elasticity is an idealization that does not take into account impurities and crystal defects in the material, among others.

Consequently, a better defined point is needed. Taking the initial elastic slope and shifting it by a specified strain offset, most commonly and here always $0.2\,\%$, an intersection of the original curve and the offset slope can be found. The stress at this point is called offset yield strength and often used as the definition for σ_{YS}.

Tensile strength, or ultimate tensile strength, refers to the maximum engineering stress that a structure can sustain. Tensile strength σ_{TS} corresponds to the peak stress, or stress at point M, on this curve. [3, p. 125]

Flow stress σ_y is a stress value used in elastic-plastic limit load analysis. Defined as the stress needed for continued deformation, flow stress takes into account the strain hardening of the material. It is usually approximated as the mean of yield and tensile strengths. [5, pp. 5–12]

2.2 HARDNESS

Hardness is a mechanical property that describes the material's resistance to localized plastic deformation. It is commonly measured by forcing a small indenter into

the test specimen. The applied force is recorded, along with the depth or size of the resulting indentation. These together give a hardness number.

There are several different hardness tests. These tests use their own units that are defined through the test method. In general, the units are only defined through their respective test methods and consequently, results from different test methods are problematic to compare. [3, pp. 134–135]

Even if hardness is defined somewhat ambiguously, hardness testing is very common for several reasons:

SIMPLICITY AND LOW PRICE

Preparation of specific specimens is generally not necessary. Also, the testing apparatus is relatively inexpensive and can be multi-purposed.

NONDESTRUCTIVITY

Especially in micro- and nanohardness testing, only a tiny indentation is left on the specimen.

COMPARABILITY TO STRENGTH

This is discussed in section 2.3. Even if the different scales are not straightforward comparable, strength can be estimated from hardness number.

REPEATABILITY IN SMALL SPACING

High spatial accuracy is easy to achieve. The test can be repeated on the same specimen as long as the indentations are not overlapping.

In heterogeneous materials such as DMWs, differences in local hardnesses are expected. As discussed next, hardness testing may provide the means for accurate local strength estimation.

2.3 CORRELATION BETWEEN HARDNESS AND STRENGTH

Both hardness and strength are properties that describe the material's resistance to plastic deformation. One might therefore expect a correlation between the two. Indeed, Pavlina and Van Tyne[6] demonstrated a linear correlation and furthermore, Jang et al.[7] showed that if the structure consists of a dissimilar metal weld, the variation in hardness and strength is similar.

The relation was also studied by Kim Wallin(unpublished) at VTT for stainless and low-alloy steels. Using this model, engineering and effective yield strengths

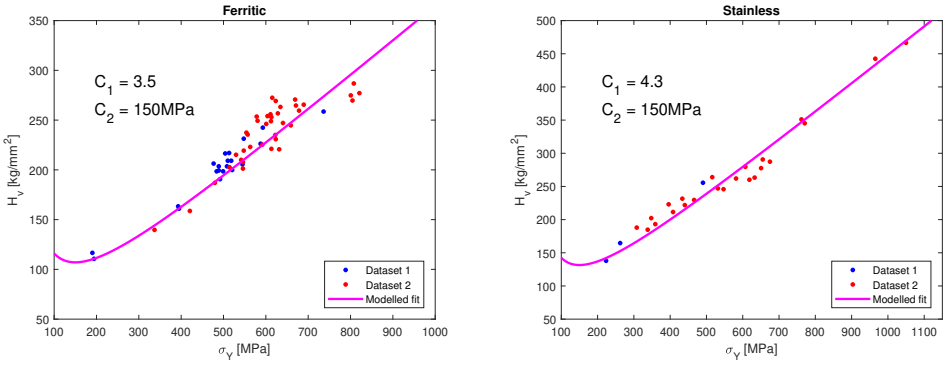

(a) Ferritic **(b)** Stainless

Figure 2: VTT model for hardness and strength correlation.

can be predicted from Vickers hardness data. The model, along with the data used to develop it, is illustrated in 2. In this model,

$$\frac{HV}{C_1} = g\sigma_y, \tag{9}$$

$$\sigma_y = \sigma_{YS}\left\{1 + \left(\frac{C_2}{\sigma_{YS}}\right)^2\right\}, \tag{10}$$

$$n = \frac{\sigma_{YS}}{C_3}, \tag{11}$$

where HV is Vickers hardness number and g standard gravity.

$C_{1,2,3}$ are modelling constants. C_1 is material dependent, proposed to be 3.5 for ferritic and 4.3 for stainless steels. The latter two were proposed to be $C_2 = 150\text{MPa}$ and $C_3 = 65\text{MPa}$. Strain-hardening exponent n corresponds with the fitting parameter in Ramberg-Osgood model.7

The model has not been tested on dissimilar metal welds but it should be just as acceptable with them, given that suitable parameters are found. As it turns out, this acceptability is in focus of this study.

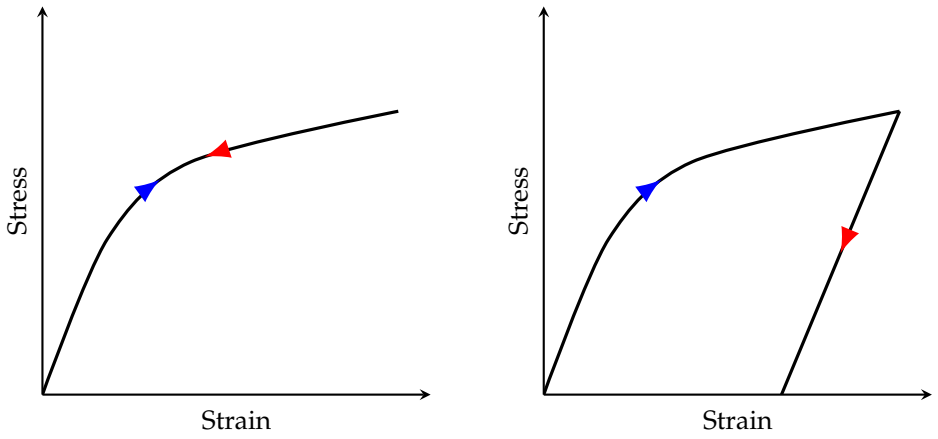

(a) Nonlinear elastic **(b)** Elastic-plastic

Figure 3: Stress-strain behaviours of nonlinear elastic and elastic-plastic materials during a loading-unloading cycle. The curves are identical during loading but follow different paths during unloading(depicted with a red arrowhead). Adapted from Anderson [9, p. 108].

2.4 J-INTEGRAL

J-integral, later referred to only by its symbol J, is a central parameter in elastic-plastic fracture mechanics. It was first defined by Rice[8] as a line integral around the crack tip in a non-linear elastic material. In plane stress or plane strain,

$$J = \int_{\Gamma} (w \cdot dy - T_i \frac{\partial u_i}{\partial x} ds), \tag{12}$$

$$w = \int_0^{\epsilon_{ij}} \sigma_{ij} \cdot d\epsilon_{ij}\,, \tag{13}$$

where w is strain energy density and ds is the length increment along the contour Γ. T_i and u_i are the components of the traction and displacement vectors, respectively. This approach is depicted in figure 4. Rice also showed that in the the nonlinear elastic zone, in other words outside the large-strain region near the crack-tip, J is independent of the path of integration.

The uniaxial stress-strain behavior of nonlinear elastic and elastic-plastic specimens are illustrated in 3. During loading they both respond similarly. The difference is evident upon unloading. The former returns along the loading path, while the latter follows a slope parallel to the linear part of the loading curve. Therefore, as long as the loading of the elastic-plastic material is monotonically rising, it can be characterized with the same parameters as the non-linear elastic one.[9, p. 107] Further knowledge of an elastic-plastic material can be obtained by studying the unloading behaviour. Such measurements are described in 4.3.2.

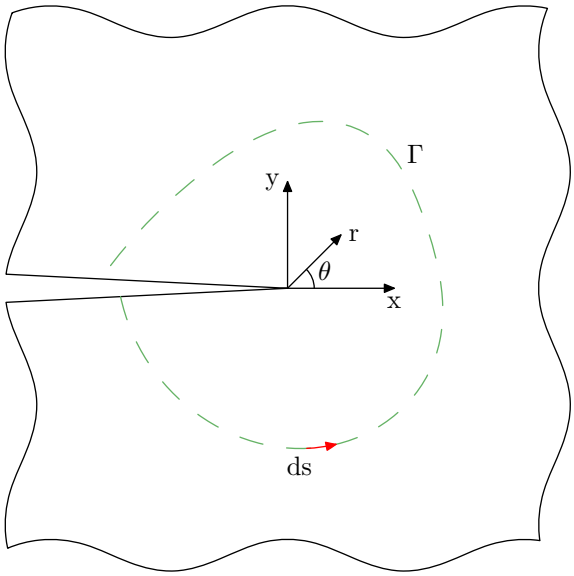

Figure 4: Visualization of the arbitrary path of J-integral around the crack tip. Adapted from Zhu [10, p. 13].

The line integral expression also establishes a linear relation between J and crack tip opening displacement(CTOD), another common measure of fracture toughness. [11, pp. 16–17]

However, Rice[8] stated that J can also be expressed in terms of change in potential energy, or energy release rate, of the material:

$$J = \left(\frac{\partial}{\partial A} \int_0^P P \, d\Delta \right)_P = - \int_0^P \left(\frac{\partial P}{\partial A} \right)_\Delta \cdot d\Delta \,, \tag{14}$$

for load and displacement controlled structures, respectively. Here, A is the crack area, P is the load and Δ is the displacement. [11, pp. 16–17]

Dimensional analysis and dividing displacement into elastic and plastic parts leads to

$$J = \frac{\eta U}{Bb} \tag{15}$$

$$= \frac{\eta_{el} U_{el}}{Bb} + \frac{\eta_{pl} U_{pl}}{Bb}, \tag{16}$$

where η is a geometry dependent, dimensionless constant, U is energy absorbed by the specimen, B is the thickness and b the remaining ligament behind the crack. Subscripts el and pl refer to the elastic and plastic components, respectively.[9,

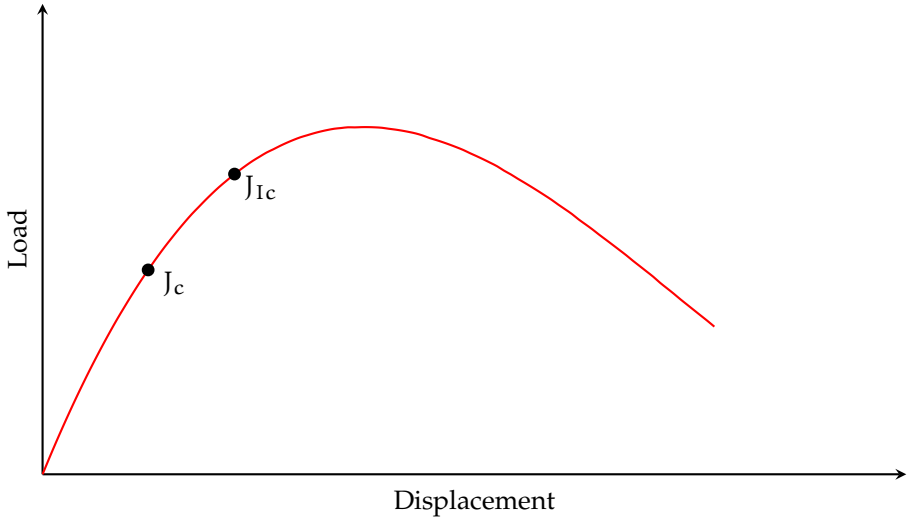

Figure 5: Illustration of fracture toughness definitions utilized. It should be noted that this is merely supposed to demonstrate where J_c and J_{Ic} are located on their respective tearing resistance curves. Their positions should not be compared to each other as they describe different phenomena. Adapted from Wallin [11, p. 37].

pp. 115–119] The elastic term can be identified to correspond with linear elastic fracture mechanics so that J becomes

$$J = \frac{K_I^2}{E'} + \frac{\eta_{pl} U_{pl}}{Bb}. \tag{17}$$

Here K_I is opening mode(i.e. mode I) stress intensity factor and E' is elastic modulus.[9, p. 119] This definition is the basis for successful methods of measuring J experimentally in E1820 and E1921, which are covered in section 4.3.

Still a question remains: at which point should J be determined? Similarly to strength, many different values have been proposed. Two of these, J_c and J_{Ic} are presented qualitatively in figure 5. J_c is calculated at the onset of cleavage fracture, while J_{Ic} refers to the value at 0.2mm ductile crack growth. [11, pp. 37–43] These quantities are further examined in chapter 4.3 and later determined from measurements.

2.5 TEARING RESISTANCE CURVE

For several reasons such as strain hardening, a material's fracture toughness can change with crack extension. Tearing resistance curve, also J-R-curve or simply R-curve, represents a material's resistance to progressive crack extension. Some

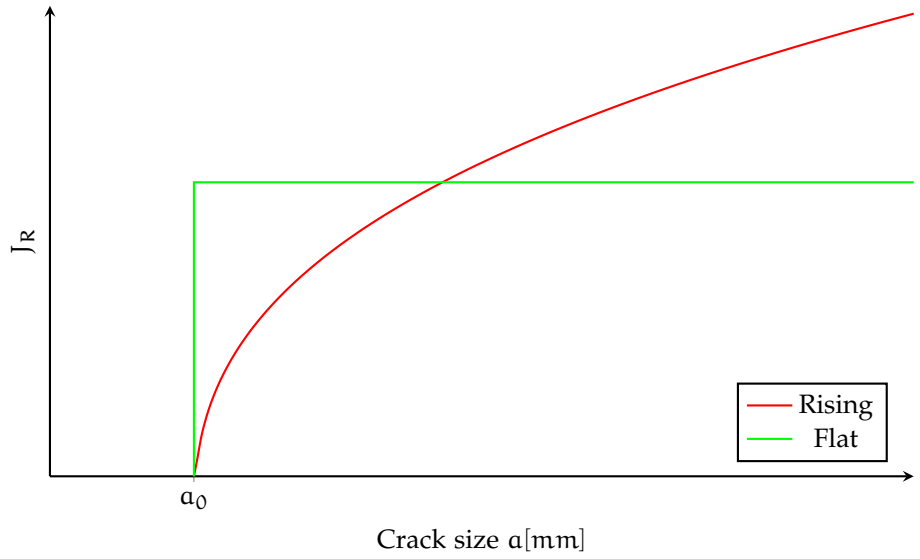

Figure 6: Schematic illustration of different tearing resistance curves. Ideally, a flat curve represents cleavage crack without any preceding ductility. On the other hand, rising curve is an example of an ideally ductile material.

possible R-curves are illustrated in figure 6. Resistance curve can be flat, falling, or rising. [9, pp. 38–40]

Curve profile depends on the fracture type. A flat curve is prevalent in cleavage fracture. Evidently this type of a curve can be described comprehensively with a single value. Ductile fracture, on the other hand, produces rising curves that are more difficult to analyze. [9, p. 231]

2.6 FRACTURE MECHANISMS AND CRACK PROPAGATION

The local crack growth resistance of depends greatly on the fracture mechanism around the crack tip. The mechanism is determined by the microstructure and temperature of the material. In the case of a DMW, the strength mismatch also has an effect on the fracture mechanism. [12]

2.6.1 Brittle fracture

Brittle fracture is an idealization of fracturing in materials that do not experience plastic deformation before cracking. In structural steels, cleavage fracture is the most common type of brittle fracture, in which river patterns are formed. These patterns can be seen in figure 16. Another brittle fracture mode would be inter-

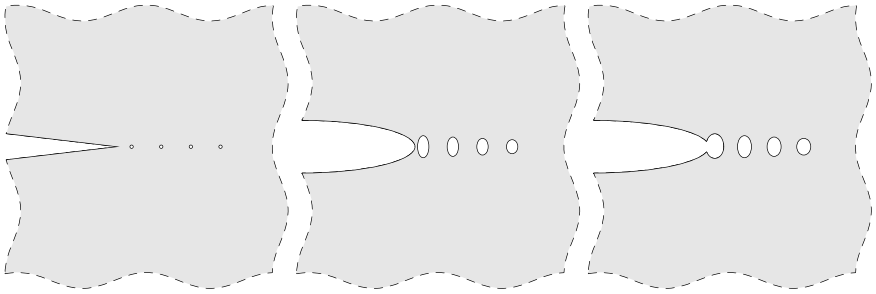

Figure 7: An illustration of ductile crack growth. Voids nucleate behind the crack front. These voids grow and eventually merge with the crack tip. Adapted from Anderson[9, p. 232].

granular fracture, which is present among others during long-term loading such as creep. [13, p. 45]

In general, brittle cracking begins once the stress is large enough to reach a microcrack behind the crack front. Therefore a statistical element emerges: the locations of the microcracks are random and naturally, ones closer to the front are easier to reach. [9, p. 237]

Brittle crack advances through the weakest path possible. Once cracking begins, the crack growth is unstable as it gets additional energy from the released elastic energy. Therefore, the crack grows extremely fast through the whole structure. [13, p. 45]

2.6.2 Ductile fracture

In the case of tensile specimens, ductile fracture occurs by plastic shear deformation. The primary mechanism for plastic deformation in metals and alloys is the movement of dislocations in the material. Dislocations are different types of defects in the crystal lattice of the material, such as impurities. [14, p. 120]

While the load of a tensile specimen is increased, eventually strain hardening cant keep up with the decrease in cross-sectional area. The specimen starts to neck. Rather than thinning out evenly across the length, the decrease in area focuses on one point. This necking could theoretically go on until sharp points break apart from each other. However, for true engineering metals, a fracture occurs at much smaller strains as dislocations enable a brittle cracking process. [9, p. 219]

On the other hand, ductile crack growth is illustrated in figure 7. The process can be divided in three stages: formation of voids around second-phase particles or inclusions, growth of the voids, and merger of the voids to form a macroscopical crack. The microstructure of the material plays a central role on which of these is

the critical step towards a failure. If the second-phase particles and inclusions are well-bonded to the primary particles, formation of free surfaces on them requires large stresses and fracture follows soon after. Then again, if the nucleation of voids requires little effort, the later stages control the ductile fracture. [9, p. 219]

Ductile growth of an existing crack produces very different circumstances than the brittle case. Local strains and stresses around the crack tip become sufficient for fracture at lower global loads. Triaxiality of the stress state generally provides enough stress elevation that void nucleation is possible. Therefore the growth and coalescence of the voids become the critical steps for crack growth. [9, p. 219]

In a through-thickness crack, the stress triaxiality is largest in the middle and crack grows the fastest there. The maximum plastic strain occurs at a 45° angle and the crack grows locally in a zig-zag pattern, although the large-scale growth stays in the original plane if the material is homogeneous. [9, p. 233]

2.6.3 Impact of temperature on fracture mechanism and fracture toughness

Specimen temperature has a profound effect on cracking. It has been discovered that ferritic steels are brittle in low temperatures and fracture by cleavage. In higher temperatures the behaviour becomes ductile and the material fails by microvoid coalescence. The region in between is known as ductile-brittle transition temperature or DBTT. DBTT is a material property and always exists if both micromechanisms are present. The actual range depends on the test method.[9, p. 247] In this context, the range can be assumed to lay in sub-zero temperatures.

The prevalence of one over the other depends on the position over the transition region. Rising temperature makes it kinetically harder to facilitate a brittle fracture and fewer microcracks are capable of it. Similarly, the lower the temperature, the more there are critical microcracks. While the crack extends through ductile tearing, more material is sampled. Eventually a critical microcrack might be found and cleavage ensues.

Above the transition temperature the fracture mechanism is clearly ductile, but temperature also has an effect the ductile fracture toughness. Namely, increasing temperature decreases fracture toughness. This effect is, however, quite insignifi-

cant. For example, Seok[15] studied A516 Gr70 steel and discovered a correlation between J_{Ic} and temperature T(in °C):

$$J_{Ic} = (-0.06T/°C + 115)kJ/m^2. \tag{18}$$

It should be noted that this does not hold when approaching phase transition temperature of around 750 °C or above. In this work, highest temperature studied is 300 °C.

3 DISSIMILAR METAL WELDS

Welding is a process in which two objects, in this case metallic, are joined together. Although immensely useful, welding presents new possibilities for defects and weaknesses, which in turn reduce the global fracture toughness of structures. Therefore, welds are a major point of interest while studying the strength of objects.

Dissimilar metal welds raise several additional issues. When joining two different alloys, a filler metal between them is usually chosen to be different from both sides. It does, however, create multiple mismatched interfaces. [16, pp. 360–361]

In this chapter, dissimilar metal welds are approached from a fracture mechanical perspective: What kind of developments occur during welding that affect the material's ability to resist fracture?

3.1 MICROSTRUCTURE

Fusion welding creates microstructurally different zones around the weld. These zones are presented in figure 8, although precise forms depend on the materials used.

While the weld pool consists mainly of the WM, some of the base metal is also required to melt and thereupon mix with the filler metal. The convection forces mixing the weld metal are weaker on the edges and material composition shifts gradually and unevenly. [16, pp. 360–362]

Element migration is also present in a DMW. As a typical and important example, post-weld heat treatment and service at elevated temperatures causes carbon to migrate across fusion line. This migration creates a carbon-depleted zone (CDZ) with reduced hardness and strength and a carbon-enriched zone, which has high hardness and strength.[18] If the join consists of a LAS base metal and a stainless steel WM, carbon migrates from base metal to the weld and a CDZ forms on the LAS side. [19]

Fusion zone (FZ) is the part of the weld that melted completely in the process. When the base metal is approached, the temperature decreases. The line from

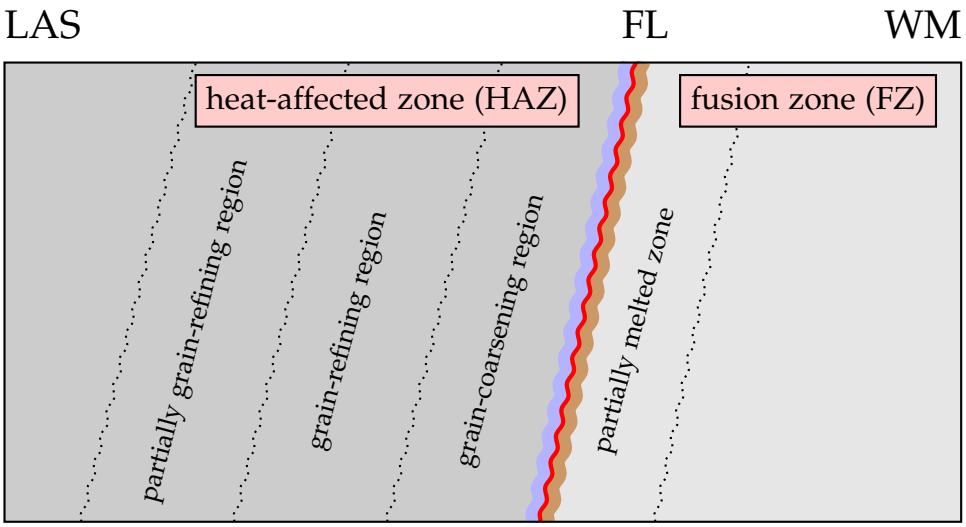

Figure 8: Schemation presentation of the different regions around a LAS-WM fusion line. Colored zones on both sides of the red fusion line represent carbon migration: brown, darker zone on the right side is the carbon-enriched zone while carbon depleted zone is marked light blue on the left. Adapted from Lindqvist[17].

which the material is completely solid is called fusion line (FL, sometimes fusion boundary FB). Yet, different alloys have different temperature ranges over which they melt. Therefore, a partially melted zone (PMZ) exists beside the fusion line.

During welding the base metal is also heated and cooled. In case of a multipass weld, this cycle is repeated. This process creates a usually 2 mm to 10 mm wide heat-affected zone (HAZ).[20, 21] HAZ extends from the fusion line to the point where heat from welding is no longer high enough to cause structural transformations in the solid.

HAZ does not consist of only one microstructure but several different ones. The final appearance depends on the chemical compositions of each part as well as the temperatures experienced. Decisive generalizations about heat-affected zones in DMWs are therefore barely meaningful.[20] Still, similar types of weldments can be expected to produce similar microstructures.

After welding, HAZ can be roughly divided into three layers. If the heat from welding causes the base metal to warm above the effective lower critical bound Ac_1, prior pearlite colonies expand during heating and break down during cooling into fine ferrite and pearlite grains. This forms a partially grain-refining region. If the temperature reaches just above the upper critical temperature Ac_3, austenite grains nucleate and cool down into pearlite and ferrite grains as well, creating grain-refining region. In the grain-coarsening region, where the temperatures rise well over Ac_3, the austenite grains grow further. These large grains and high cooling rate support the formation of Widmanstatten ferrite on the grain boundaries. [22]

The A508 LAS base metal has been previously identified as having initially a bainite microstructure.[12, 19] The same goes for 18MND5.[21] Right next to the FL on the HAZ side, a thin martensitic layer may form. [19, 23]

Other types of defects are also possible. These defects include lack of fusion between weld beads or weld bead and the base metal as well as second-phase inclusions.[24, p. 285] These phenomena and their effects, however, are not in focus here.

3.2 STRESS AND STRAIN BEHAVIOUR

Residual stresses are any mechanical stresses that exist when no external load is present. Welding has a profound effect on the residual stress state. First, the thermal expansion and contraction cycles are not homogeneous as different temperatures are reached throughout the weld. Also, phase transformations such as γ to α may occur. Such transformations come with residual stresses due to a change in volume.

Residual stress states in dissimilar metal welds are even more complex. The mismatch in mechanical properties raises further issues, when different thermal coefficients cause uneven contraction during solidification. [25, pp. 75–79]

Aside from the residual stresses, the various zones and microstructures around the weld may exhibit other changes in strength. For example, the aforementioned carbon migration causes a loss of strength in the LAS and an increase in the hardness of the WM. [19] Furthermore, the lath martensite found in the HAZ near the fusion boundary is harder than surrounding microstructures.

Generally all engineering steels are work hardened or otherwise strenghtened before application. The strength increase is achieved through changes in the crystalline structure. In the fusion zone such changes are lost completely as the material melts and recrystallizes during cooling. In the HAZ the loss is not complete but still remarkable. [16, pp. 514–515]

It should be noted that a post-weld heat treatment can resolve some of these issues, by relieving residual stresses and recrystallizing the microstructure.

Overall, the local and complex microstructures cause local fluctuations in mechanical properties of a weld. Ferritic-austenitic DMWs have been found to be weaker in fracture resistance than similar welds of either type. These welds with Alloy 52 as the filler metal have been studied on several occasions. [12, 19, 23, 26] All these

studies agree that the highest strength and hardness along with lowest ductility and toughness is found in the HAZ of the LAS near the fusion boundary. In fact, the peak is quite remarkable and the largest strength mismatch is visibly here. Furthermore, this zone exhibits smallest tearing resistance and is therefore the most prone to failure.

The characteristics of weldments such as residual stresses put them at risk of brittle fracture. [9, p. 334] At the same time, the HAZ of an overmatched weld is susceptible to fracture by cleavage due to very high ductile fracture resistance. [17, p. 17] Nevertheless, both brittle and ductile fracture mechanisms are possible in general and the actual mechanism depends on the specifics of the material and its circumstances. Wang et al.[12] observed also that mixed ductile and brittle fractures occur in the interface zones.

3.3 CRACK PROPAGATION AROUND TO THE LAS–WM FUSION LINE

Sections 2.6.1 and 2.6.2 described that global constraints force cracks to grow straight in normal conditions. However, if a region adjacent to a crack is weaker than the initial crack path, the crack may grow out-of-plane. Wang [12] and Lindqvist [17] have reported that while cracks grow straight in the base metal as well as in the WM of an Alloy 52 DMW, a crack in the HAZ propagates towards the fusion line. This suggests that the material is weakest along the fusion line.

Since cracks may deviate from the original plane towards a weaker microstructure, it is not a stretch to suggest that such behaviour might have an effect on the fracture toughness of the material. Several reports[12, 27, 28] have been written for ductile and mixed fractures. They suggest that cracks near the fusion line exhibit deviation from the original plane and fracture toughness is the lowest there. However, brittle fracture has not been investigated before.

It should also be noted that the distance from the crack to the FL may vary, particularly if the weld beads form a fluctuating fusion line or the crack is diagonal to the fusion line. This means that a jump towards the fusion line may not happen immediately, but only after the distance has decreased enough. An example can be seen in 9, where the fusion line gets closer to the original crack plane as the crack grows.

4 METHODOLOGY

In this thesis I utilized research data from earlier projects done at VTT and supplemented them with my own measurements. This chapter focuses on the methods used to obtain data. The specific procedures are described in chapter 5.

4.1 DATA COLLECTION AND DIGITIZATION

Some of the data used was obtained by digitizing information from previous projects. optical microscope (OM) fractographs of cross-cuts had been used only qualitatively. Now, quantitative research meant that images needed to be transformed into numerical data. An example is presented in figure 9. Once the digital images had been collected, Origin software was used for digitization. Points were picked manually and transformed to correct axes. The path traced by these points was then scaled and saved to be later analyzed in MATLAB.

4.2 HARDNESS TESTING

As discussed before, hardness testing can often be advantageous. American Society for Testing and Materials (ASTM) has published a standardized Vickers hardness test method in E384[29]. The Vickers test is a hardness test with one of the widest scales of applicability. It uses a diamond indenter with the shape of a square pyramid. The indenter is forced into the specimen with controlled force and ideally a symmetrical dent ensues. This indentation is measured under a microscope. The Vickers hardness number is the defined as:

$$HV = 0.0018544 \times F/(\frac{l_1 + l_2}{2})^2, \tag{19}$$

where F is the applied force and l_1,l_2 are diagonal lengths of the indentation.

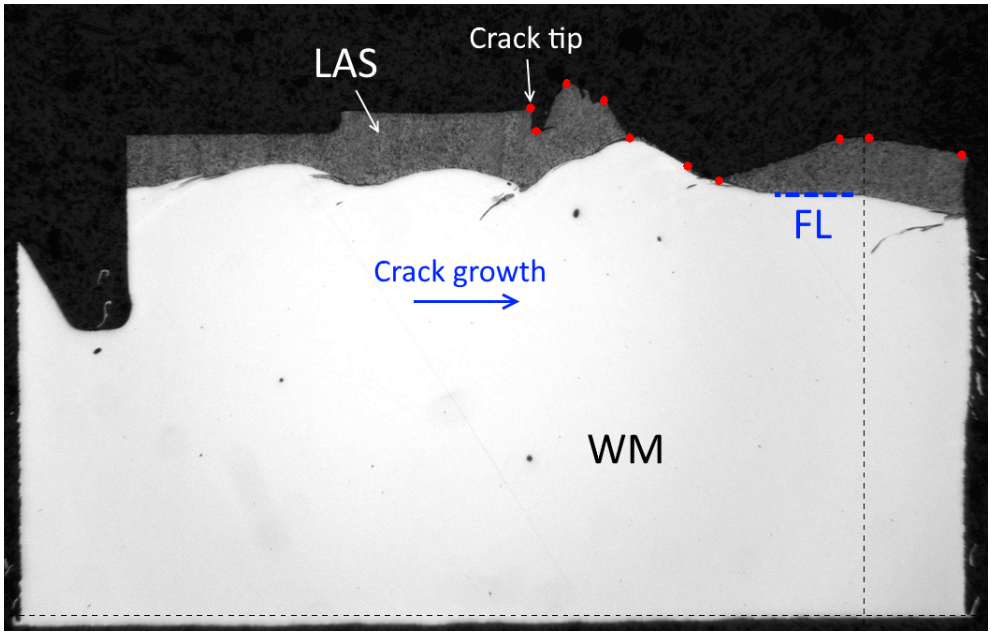

Figure 9: An example of digitized data from an OM fractograph. Red dots illustrate the manually traced crack path. This particular specimen is MU1-E10.

4.3 FRACTURE TOUGHNESS TESTING

While J-integral is accepted as a unit of fracture toughness, further details are needed for appropriate testing. Different circumstances, namely brittle and ductile fractures, require different test methods. Consequently distinct values of J are used. ASTM standards E1820 [30] and E1921 [31] define test methods to measure J_{Ic} and J_c, respectively.

Even if the final values differ, calculation procedures for J from load-displacement curves are quite similar. The principle is illustrated in figure 10. Once a curve has been collected, the area below it is divided into plastic and elastic parts. In case of an elastic compliance method, such as the one used here in E1820, the dividing slope corresponds with the measured loading-unloading slope. On the other hand, in E1921-style brittle fracture, the division is done parallel to the initial slope.

Elastic area value is only useful for determining the plastic one from total, as the elastic J_{el} can already be established from linear elastic fracture mechanics. Plastic area, however, allows the calculation of plastic J_{pl}. This depends on the test method and the specimen configuration, which will be discussed next.

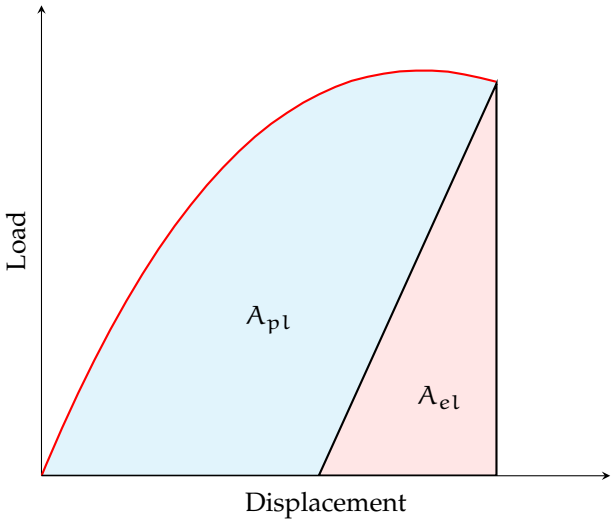

Figure 10: Principle of calculating J. Adapted from ASTM E1921[31, p. 13].

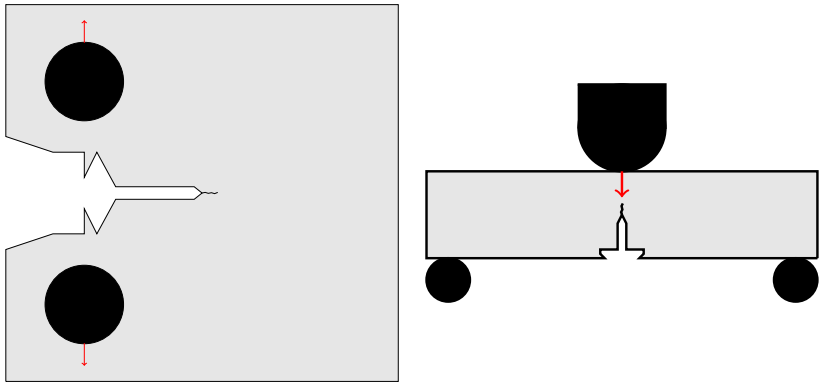

(a) C(T) **(b)** SE(B)

Figure 11: Different specimen configurations. Red arrows indicate loading directions. The actual shape of the machined notch in front of the crack varies.

4.3.1 Specimen configurations

Toughness testing was touched upon in the beginning of chapter 2. The specific method of measuring load and displacement, however, depends on the specimen configuration. There are a couple of different shapes of specimens used in fracture mechanical testing, all of which have their advantages and disadvantages. Two types are used here and presented in figure 11.

The fracture mechanical parameters studied here are defined as material properties. That is, the parameters should be independent of the varying geometries of cracking objects as long as the stress state is similar. Wallin[11] suggests, however, that this might not be the case in either brittle or ductile fracture. For these reasons it might be a stretch to assume that comparison of different geometries' properties is unambiguous.

The differences between C(T) and SE(B) specimens are largely known and mostly taken into account in the standards. The tearing resistance key-curves of C(T) specimens are slightly flatter than comparable ones for SE(B) specimens. [11, p. 108]

Different specimen geometries also provide a challenge. Stress state triaxiality, or the plastic constraint, of a specimen might be compromised in some cases. This is a concern for both brittle and ductile fracture. Additionally, cleavage fracture requires a nucleation point such as a microcrack behind the crack front, as discussed in section 2.6.1. Naturally such point is more readily available in a bigger specimen.[11, pp. 57–58] For ductile crack growth, the variation in load-displacement curves grows as the size decreases. [11, p. 108]

4.3.2 Ductile fracture toughness

Ductile fracture testing is done by determining the tearing resistance curve and key parameters from it. There are both single and multi-specimen techniques. Generally speaking, the multi-specimen technique is simpler and requires less sophisticated equipment. If done accurately, it also gives the most reliable measure of tearing resistance. On the other hand, single specimen methods are faster, less expensive and well suited for automation. They also eliminate the error rising from variance between specimens. [11] For the above reasons, single specimen partial unloading technique is the most commonly used method.

ASTM standard E1820[30] defines a test method for measurement of J_{Ic}, which represents elastic-plastic fracture toughness in plane-strain conditions around the crack tip. The standard allows the application of certain types of both single and multi-specimen techniques. One of them is elastic compliance method, also known as partial unloading method. It provides the means to obtain a complete tearing resistance curve from a single specimen, enabling the calculation of J_{Ic}. [30]

Before testing, a sharp pre-crack must be produced in the crack front. This helps to ensure that the crack grows straight and in the preferred direction. Furthermore, to establish a desired path for the pre-crack, a starter notch is machined. This notch is created by periodic loading well below the fracture toughness of the material for about 10^4 to 10^6 cycles. [30]

The elastic compliance method is illustrated in figure 12. The specimen is sequentally unloaded and reloaded. Each cycle provides an estimate of the specimen compliance and crack length. First cycles are made with forces smaller than the precrack-

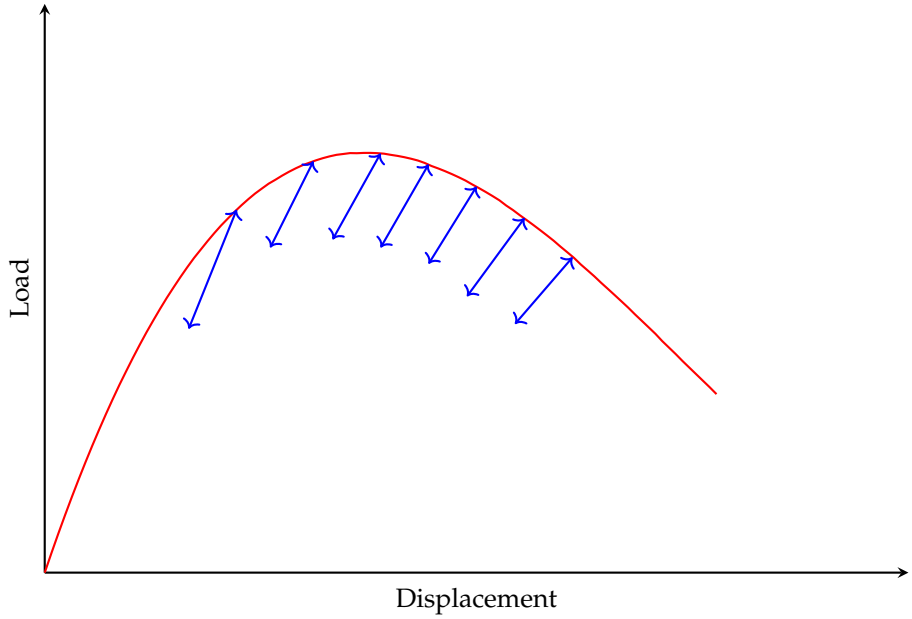

Figure 12: The principle of elastic compliance method. Red line depicts a typical stress-strain curve for a ductile material. Blue lines indicate the partial unloading-reloading cycles. These cycles provide tearing resistance data as in figure 13. Adapted from Wallin [11, p. 52].

ing force to estimate the original crack size. During the primary testing, unloading cycles produce crack extension estimates. Along with corresponding J values, these estimates can then be used to determine the tearing resistance curve. [30]

An illustrative tearing resistance curve is pictured in figure 13. A blunting line is constructed using flow strength σ_y. Then, parallel lines are drawn. Between these offset blunting and exclusion lines lies acceptable data, although additional conditions apply. [30]

Next, a regression line of the following form is established:

$$\ln J = \ln C_1 + C_2 \ln\left(\frac{\Delta}{k}\right), \tag{20}$$

where $k = 1.0\text{mm}$ and C_1, C_2 are fitting parameters[30].

Once the regression line has been established, if the data meets a set qualifications, the intersection of the regression and offset blunting lines indicates J_{Ic}. [30]

In order to construct a blunting line, tensile tests are required to measure σ_y unless textbook values are implemented. In either case, uncertainties in σ_y have a profound effect on J_{Ic} as the slope of the blunting line changes.

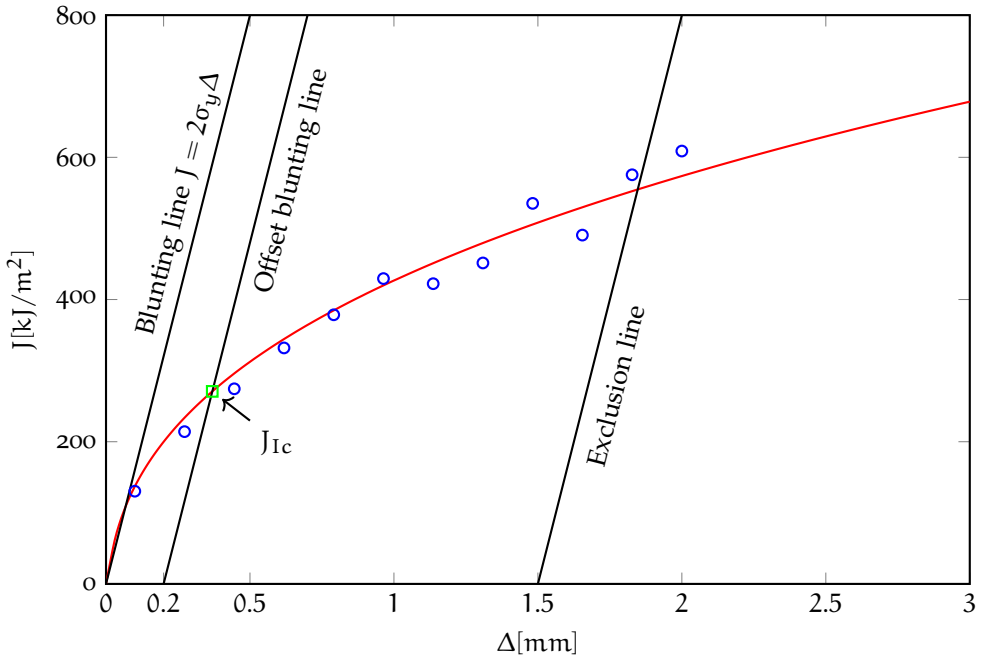

Figure 13: Typical tearing resistance curve for a ductile metallic material. Blue dots indicate measured values obtained from unloading-loading cycles as in 12. Red line is a fit to this data. Blunting line is used to construct offset blunting and exclusion lines. Green square indicates the intersection from which J_{Ic} is determined. Adapted from ASTM E1820 [30, p. 31]

.

4.3.3 Brittle fracture toughness

ASTM E1921 defines a test method to determine master curve reference temperature T_0 in the transition range. Consequently, it defines a method to determine brittle fracture toughness J_c. The standard is actually defined only for homogeneous materials as the path independence of the J-integral is compromised in multi-component materials such as dissimilar metal welds. [31, p. 1] It has been proven by Blouin et al. [32], however, that if the integration path is large enough and plasticity small compared to the specimen dimensions, path independence is preserved and J_c remains a valid measure of fracture toughness.

Master curve testing commonly searches for a temperature sweet spot to determine T_0. Consequently each dataset separately converges to a test temperature, where remainder of the tests is committed.

In the transition range the specimens eventually crack by cleavage. From the load-displacement curve, J_c is calculated at the onset of this cleavage fracture. Cal-

culation of J_c follows the formula introduced in equation 17. The elastic part is calculated with the elastic stress intensity factor K_e:

$$J_{el} = \frac{(1-\nu^2)K_e^2}{E}, \tag{21}$$

where ν is the Poisson's ratio and E is the elastic modulus. While these two are material properties, K_e is dependent on the specimen geometry. [31, p. 13]

The plastic component is calculated from energy absorbed U_{pl} by the specimen, which corresponds with the plastic area under the load-displacement curve A_{pl} as in figure 10:

$$J_{pl} = \frac{\eta A_{pl}}{B_N b_0}, \tag{22}$$

where η is a dimensionless parameter, B_N the net thickness of a side-grooved specimen, and b_0 the initial remaining ligament. [31, p. 13]

4.4 CRACK PATH PROFILING

In order to determine whether a crack propagated to the fusion line, the crack path has to be studied. Two different techniques were used, cross-cut imaging and optical profilometry.

In cross-cut imaging the fractured specimen is cut along a line parallel to the sides. This cross-cut section is then scanned with an OM. These fractographs can then be digitized as described in 4.1.

In optical profilometry the fractured specimens were profiled using an optical microscope Sensofar PLμ2300 that utilizes interferometry and confocal techniques.

Irregularities in a surface create phase shifts in reflections which in turn can be identified in the interference patterns. Interferometry utilizes these patterns by studying the surface on several different wavelengths. [33]

Confocal microscopy seeks to improve image quality by employing a pinhole aperture. The light illuminating the surface is directed through the aperture so that only the focal point is illuminated and noise emerging from the surrounding area is minimized. From there on the surface is scanned serially and the image is constructed one pixel at a time. [34]

4.5 SCANNING ELECTRON MICROSCOPY

Close inspection of the crack surface is done with a scanning electron microscope(scanning electron microscope (SEM)). Compared to OM, SEM is able to produce up to 1000 times better magnification with an ultimate resolution of 1 nm. [35]

In SEM, an electron beam is emitted towards the surface. The interaction between the electrons and the surface produces various detectable signals such as secondary, backscattered and auger electrons, as well as x-rays. [35] Combining these signals allows the user to construct a detailed image of the surface. In the case of a cleavage fracture surface, such detail enables the investigation of river patterns to determine the original crack nucleation location.

5 MEASUREMENTS

This chapter introduces the materials as well as pre-existing data and describes in detail the measurements and analysis methods utilized in this thesis.

In short, the data of this study was obtained through hardness and tensile measurements, fracture toughness measurements (both brittle J_c and ductile J_{Ic}), as well as cross-cuts and profiles of the associated fracture surfaces. Some of the data was gathered from previous projects. Associated reports are referred to with the corresponding measurements.

Measurements for this study included profilometry of previously fractured specimens. Additionally, nucleation points of brittle fractures were sought with SEM and profilometry was validated with cross-cuts and OM.

5.1 TEST MATERIALS AND SPECIMENS

Tested specimens are listed in table 1. Two different mock-ups were studied here: MULTIMETAL(MU1) and NIWEL(NI1). Both DMWs were narrow-gap(NG) welds. The chemical compositions for each material used are listed in table 2. The manufacturing and test specimen preparation of MU1 and NI1 are described in detail in [17, pp. 39–45] and [36], respectively.

Table 1: Test matrix for measured specimens. In NIWEL specimens the prefix tells the thermal ageing condition: 'AS' for as received, 'V' for 5000 h and 'K' for 10 000 h.

Project	Specimen(s)	Dimensions	Measurements
MULTIMETAL (MU1)	H1	Single large	HV
	Y[1-12]	Miniature tensile	σ_{YS}, σ_{TS}
	[A-E]10	10x10 SE(B)	Cross-cuts, J_{Ic}
	[A-D]20	10x20 SE(B)	Cross-cuts, J_{Ic}
NIWEL (NI1)	BR-AS[1-15] BR-V[1-15] BR-K[1-15]	5x10 SE(B)	Profiles, J_c
	DU-V[1-5] DU-K[1-5]	25x50 C(T)	Profiles, J_{Ic}

Table 2: Chemical composition of mock-up materials. Iron balances the composition to 1.

	C	Cr	N	Ni	Ti	Si	Mn	S	P	Mo	Cu
316L	0.03	16-18	0.10	10-14	x	0.75	2.0	0.03	0.045	2-3	x
Alloy 52	0.04	28-31.5	x	58.5	1	0.5	1	0.015	0.02	0.5	0.3
18MND5	0.175	0.18	x	0.64	x	0.245	1.55	0.002	0.008	0.495	0.13
SA508	0.19	0.17	x	0.82	x	0.08	1.35	0.002	0.006	0.51	x

MU1 consisted of SS base metal 316L, LAS base metal 18MND5 and weld metal Alloy 52. The weld metal was undermatched($M = 0.79$) on the LAS side. On the other hand, NI1 consisted of the same SS base metal and weld metal as MU1: 316L and Alloy 52, respectively. LAS base metal was Grade 3 SA508.

Both materials were manufactured with gas tungsten arc welding(GTAW) and post-weld heat treated(PWHT), first at 550 °C for 15 h and then at 610 °C for 8 h. NI1 was additionally studied in three different ageing conditions: I) As-welded PWHT condition, II) 5000 h aged and III) 10 000 h aged. Ageing was done in an air furnace at 400 °C. As-welded ductile NI1 specimens could not be utilized here as they had been consumed by previous studies.

5.2 HARDNESS AND STRENGTH OF NG-DMWS

Hardness testing procedure is described in detail by Lindqvist[17, pp. 32–33]. In short, hardness testing was made with the Vickers technique in accordance to ASTM E384. Testing was done in nine lines across the Alloy 52 LAS - fusion line. Applied force was 1 N.

In order to study the correlation of hardness and strength, tensile properties were tested as well. The testing procedure is described in detail by Lindqvist[17, p. 47]. An increasing load was applied to specimens. The stress and strain were recorded, which in turn enabled the determination of σ_{YS} and σ_{TS}.

5.3 CRACK PATH AND DUCTILE FRACTURE TOUGHNESS

J_{Ic} measurements done to MU1 and NI1 specimens are described by Lindqvist[17] and Ahonen et al.[36], respectively. In a nutshell, the specimens were cracked in

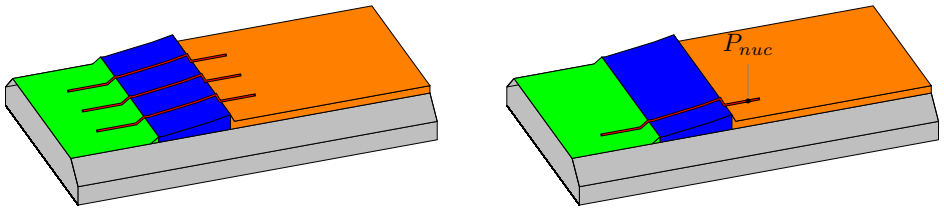

(a) Ductile case. Three paths were profiled from each specimen.

(b) Brittle case. P_{nuc} shows the brittle fracture nucleation location. Red line with black outline shows the profiling path, which runs through P_{nuc}.

Figure 14: Illustrations of profiling paths for brittle and ductile specimens. Green area is the machined notch, blue zone is the fatigue pre-crack and orange zone is the actual crack face. Red lines correspond with the profiling paths.

room temperature and load-displacement curve was examined as described in section 4.3.2.

Crack paths were profiled using the methods described in section 4.4. MU1 were studied using cross-cuts, NI1 by means of profilometry. NI1 specimens were attached to the microscope base using suitable adhesive. Microscope lens was Nikon 20x. 12 mm long paths were profiled from three different points as illustrated in figure 14a. The width of the specimen was observed and profiles were measured from equal distances to each other and the sides.

A representative crack profile with corresponding analysis is depicted in figure 15. The beginning of the data includes a portion of the machined notch in front of the crack. All points were rotated so that the abscissa runs parallel to this notch. The peak around the end of pre-crack was then identified as the pre-crack tip.

The possible jump towards the fusion line happened during the first 1 mm of the crack in the original plane. Therefore, distance to fusion line d was quantified as the largest vertical distance between the initial crack plane and the fusion line in this range. Three profiles were measured from each specimen to evaluate the precision. From these three measurements, mean and deviation from mean of d were calculated for each specimen. Acceptability of profilometry in general is studied and confirmed in the next section utilizing brittle fracture specimens.

5.4 CRACK PATH AND BRITTLE FRACTURE TOUGHNESS

Fracture toughness measurements made for NI1 specimens are covered by Ahonen et al.[36]. In short, the specimens are cracked in a reduced temperature around the DBTT(see section 2.6.3). The analyzation follows the method outlined in 4.3.3.

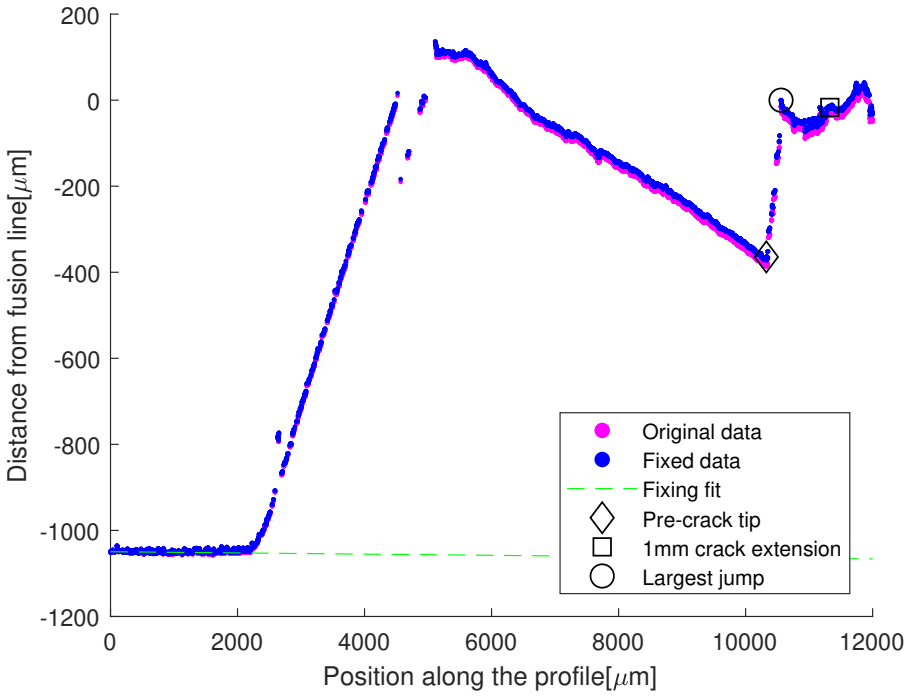

Figure 15: An example of a ductile crack profile. Essential processing is also illustrated.

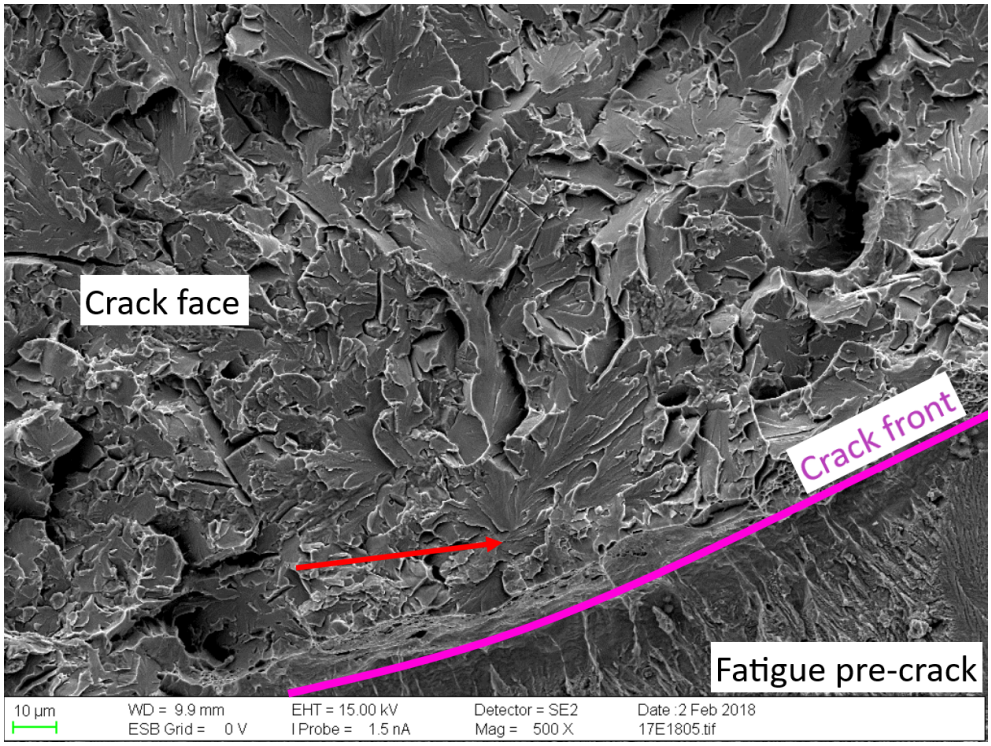

Figure 16: One of the SEM fractographs of a brittle crack front. Red arrow indicates the observed nucleation point, from which brittle fracture "rivers" emerge.

Nucleation point of cleavage crack propagation was identified using SEM. Figure 16 shows an example of an identified nucleation point. The point was identified from the river patterns that converge there.

The specimen was then profiled using Sensofar PLμ2300 profilometer. Microscope lens was Nikon 50x and step size of the objective was 0.4 μm. The specimen was mounted to the microscope with putty so that the crack face was normal to the lens and straight in the x-y plane.

The profiling path is illustrated in figure 14b and a sample measurement is presented in figure 17. The length was determined to be long enough to accompany both the nucleation point and part of the machined notch in front of the crack. The notch is assumed straight, so it can be used to estimate a horizontal line even if the specimen was loaded unevenly.

Accuracy was estimated by profiling six specimens five times. The procedure is illustrated in figure 18. There were some measurements that differed significantly from the mean. This was most probably caused by a human error during measurement process, either in the set-up or the profiling line positioning. Such values were discarded. The measurements were independent and thus follow normal distribution as per central limit theorem. Hereafter, new means and their standard errors were calculated. A linear fit was performed and a parallel line encompassing all errors constructed. Finally, $3\,\mu m + 0.5\,\%$ was accepted as the error estimate.

Human error discussed earlier was reduced by repeating measurements for each specimen. If the paths recorded had more variation than most others, another repeating measurement was made. Then, the profile most different from others was discarded and the mean of the accepted measurements was used.

Overall acceptability of the method was examined by cutting cross-sections from three specimens(one from each thermal ageing group) and comparing OM fractographs from them to profilometry data. An example of this comparison is illustrated in figure 18. It was established that the cracks indeed jump to the fusion line and the distance measured with the profilometer is consistent with a cross-cut. In the particular example illustrated, NI1 specimen BR-K13, cross-cutting gives $d_{cc} = 146\,\mu m$, whereas the mean of the profiles was $d = 150\,\mu m$. The difference is smaller than the estimated uncertainty and quite small in general.

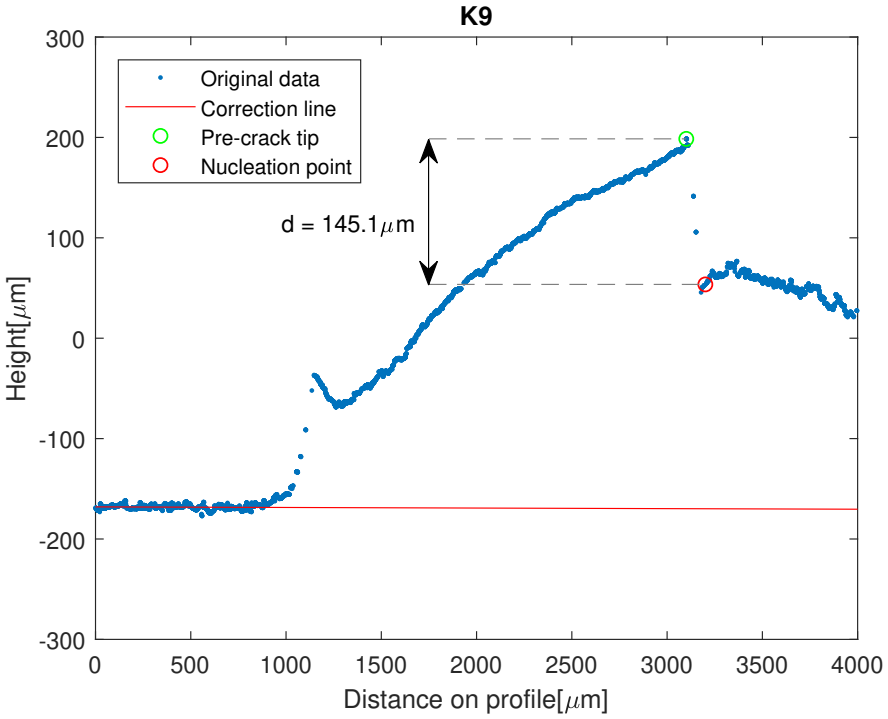

Figure 17: An example of a brittle crack profile. Nucleation point is located at a distance from the crack tip determined with SEM .

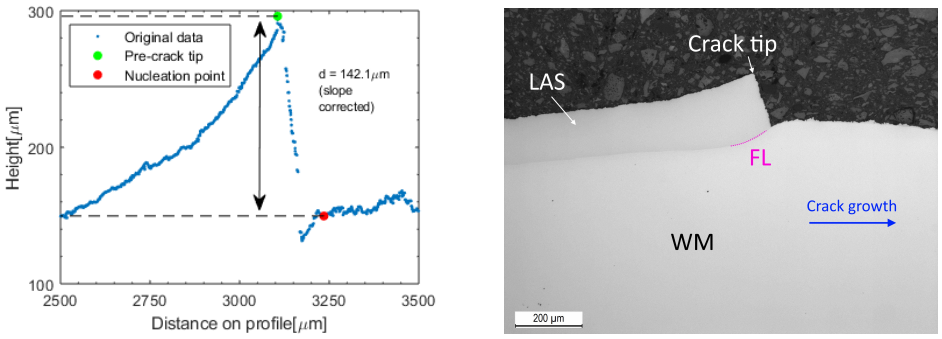

(a) Profilometer

(b) Cross-cut examination

Figure 18: A magnification of verification around the crack tip. Both methods record similar shape and distance from crack tip to fusion line. The specimen in question here is NI1 BR-K13.

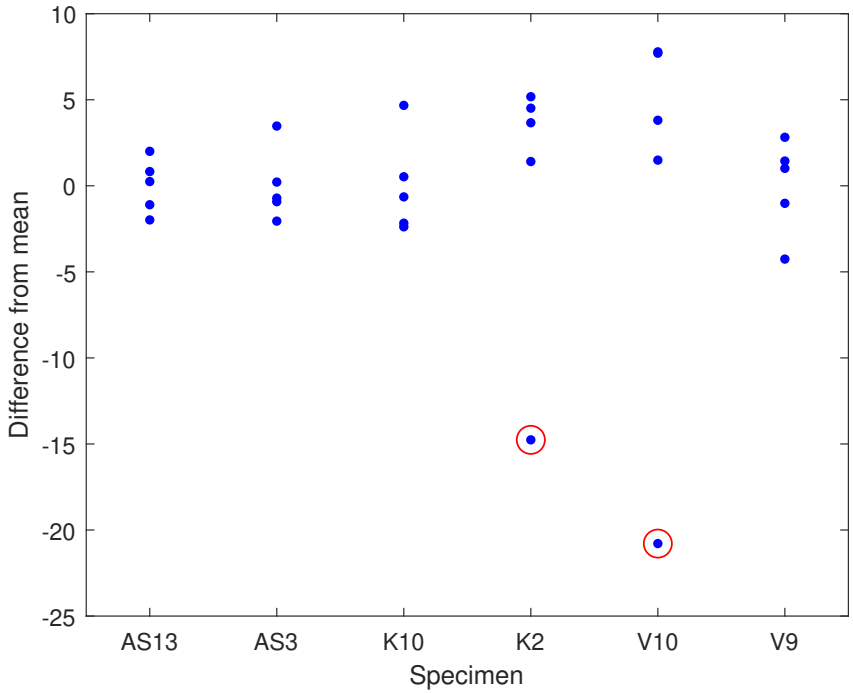

(a) Measurements' difference from mean for specimens selected for error estimation. Ones circled with red are considered faulty measurements and are discarded.

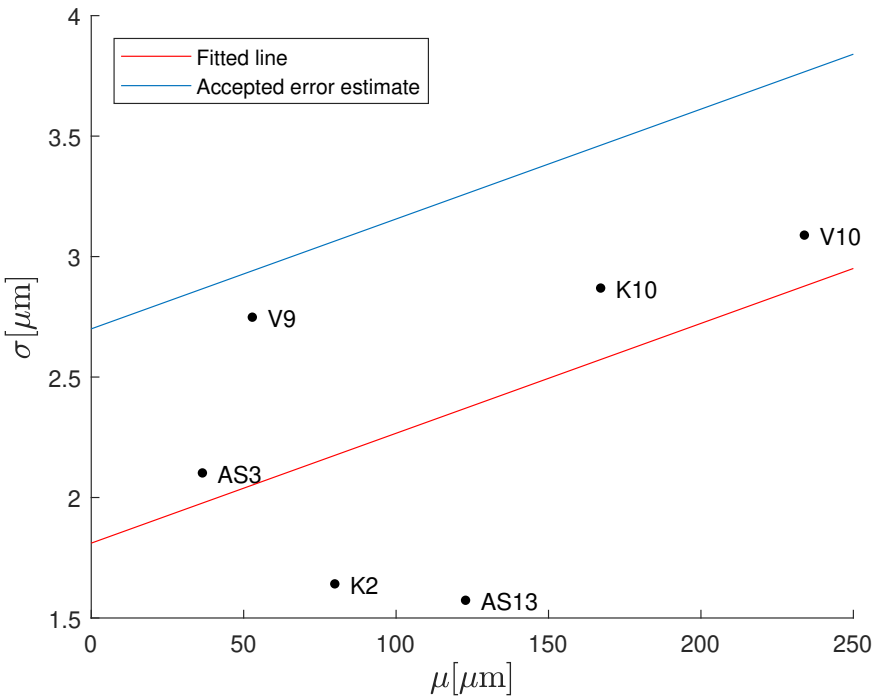

(b) Standard errors of the mean compared to the means once the outliers have been discarded. Red line indicates is a linear fit. Blue line is the accepted error estimate.

Figure 18: Error estimation of brittle fracture crack propagation.

6 RESULTS AND DISCUSSION

6.1 HARDNESS OF AN ALLOY 52 DMW

The Alloy 52 DMW hardness data from MU1 is illustrated in figure 19 along with the medians and their error estimates. The data is split into equally sized intervals of approximately $0.1mm$. This illustrates how much closer inspection of local mechanical properties is possible by studying hardness than by tensile testing.

A simple observation makes it clear that the hardness measurements at each distance are skewed to the upper bound and the distribution is not clear. In this case bootstrapping the data and calculating the mean of bootstrapped medians was considered a sound approach to estimate hardness. On the other hand, minimum hardness could also correlate with tensile and fracture strengths. The mean and minimum values were therefore further examined.

There are clear differences in hardness adjacent to the fusion line. LAS side exhibits much larger variation than the weld metal. There is a peak in hardness in HAZ near the fusion line. These traits have been identified and explained in previous studies[17, 19, 26] and discussed in section 3.2. In the WM side, hardness stays constant with notably less deviation. Particularly the median values are almost independent of d.

It can also be anticipated that the minimum values have too much randomness for proper estimation. Naturally such randomness is not meaningless as it may express the inhomogenuity of the material. As a statistical predictor, however, extreme values a rarely optimal. It is impossible to tell whether the minimum value of the sample represents 5 %, 1 %, or 0.01 % of the real distribution. Therefore it is unlikely that tensile properties could reliably be predicted from them.

As a sidenote, further studies on the distribution of measured hardnesses could prove interesting. There seems to be clear differences around the FL and knowledge of the distributions would help in strength correlations, among others.

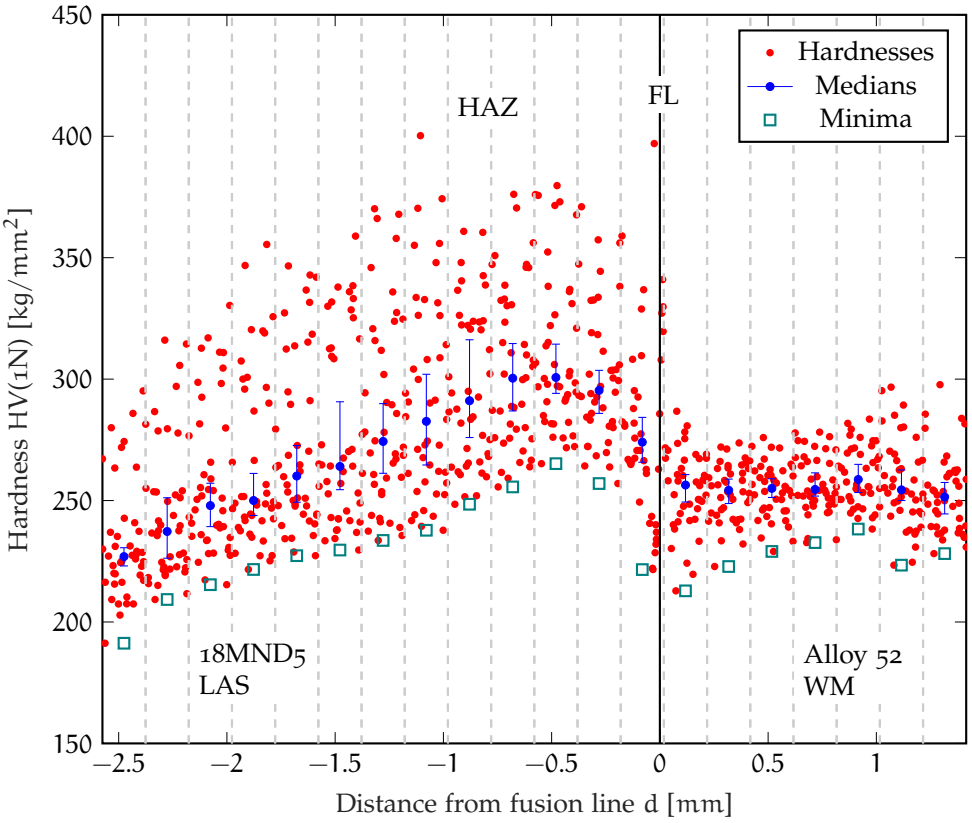

Figure 19: Results of hardness testing of DMW on the LAS border. Dashed vertical lines illustrate the chosen spacing for averaging the data. Blue points are means of bootstrapped medians from the interval, along with 95% confidence intervals. Cyan squares indicate minima between each line.

6.2 HARDNESS AND STRENGTH CORRELATION FOR AN ALLOY 52 DMW

Correlation between hardness and strength was studied with the hardness data presented in the previous section. On the LAS side, tensile tests were performed 2 mm, 0.5 mm, and 0 mm away from the fusion line, three on each. In figure 20, the yield strengths from these tests are matched with the corresponding Vickers hardness measurements. The original ferritic VTT model as in figure 2a is plotted alongside. On the WM side, tests were performed 1 mm away from the fusion line.

In figures 21 and 22, the VTT model is applied to predict strength from hardness. All measured and predicted yield and tensile strengths are presented.

Minimum hardnesses are utilized in figure 21. The prediction curve alternates over and under the measured strengths. It seems that the variance in the minima is too large to be practical, as predicted in previous section. Therefore, the minima are excluded from further analysis.

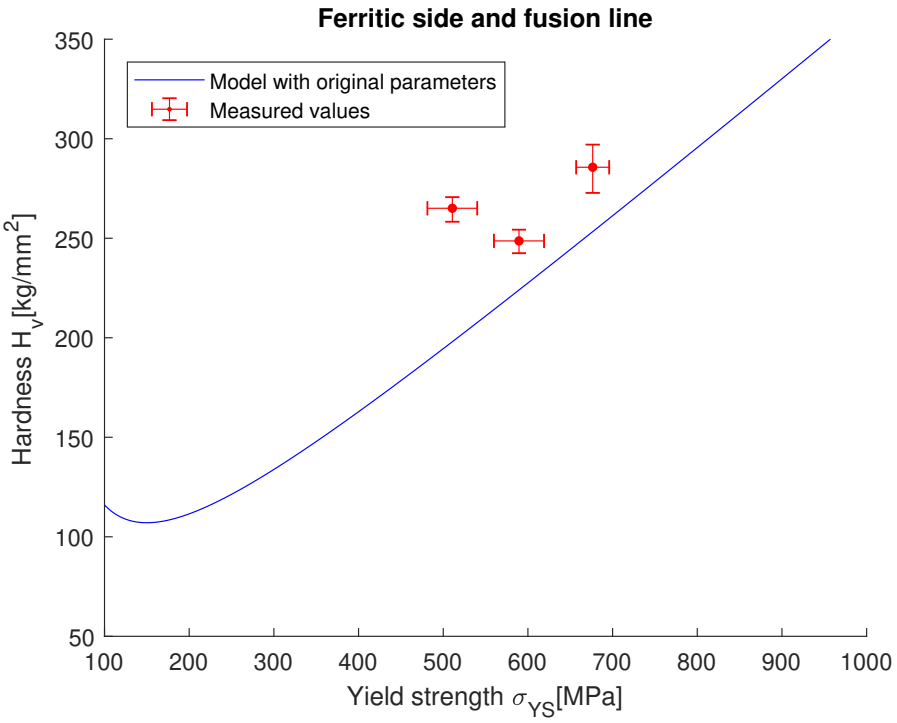

Figure 20: VTT model for LAS side with results from tests. Curve is identical to the one in figure 2a. Applied force in the hardness measurements was 1 N.

The median values in figure 22 provide a more consistent curve, although the original parameters seem to miss the mark by some margin. Better parameters were discovered by varying the parameters and minimizing Pearson's χ^2-test. If the parameters are varied, the predictions are quite agreeing with measurements.

To summarize, it appears that the VTT model could be used for predicting local strength of a DMW from hardness data on a distance scale that is impossible to measure with tensile testing. Yet, the original parameters do not work well with the investigated material. A good approach seems to be to perform some tensile tests in addition to the hardness measurements in order to determine better parameters.

Naturally, supplementary measurements could prove that the parameters used here are generally acceptable for dissimilar metal welds of this type. Additional testing with varying materials would be needed for verification.

Some other improvements could also be considered. Elastic moduli of different steels are quite similar and well known, ranging roughly from 190 to 220 MPa. Here textbook values for elastic modulus E of each alloy were used so that E on the fusion line was the average of both sides. However, the inhomogeneity of the weld may make this estimation too robust. Proper estimations could be made, for example, with Oliver-Pharr loading-unloading variant of hardness testing. [37], [38] Hardness testing with different loads could also provide additional information as it has been

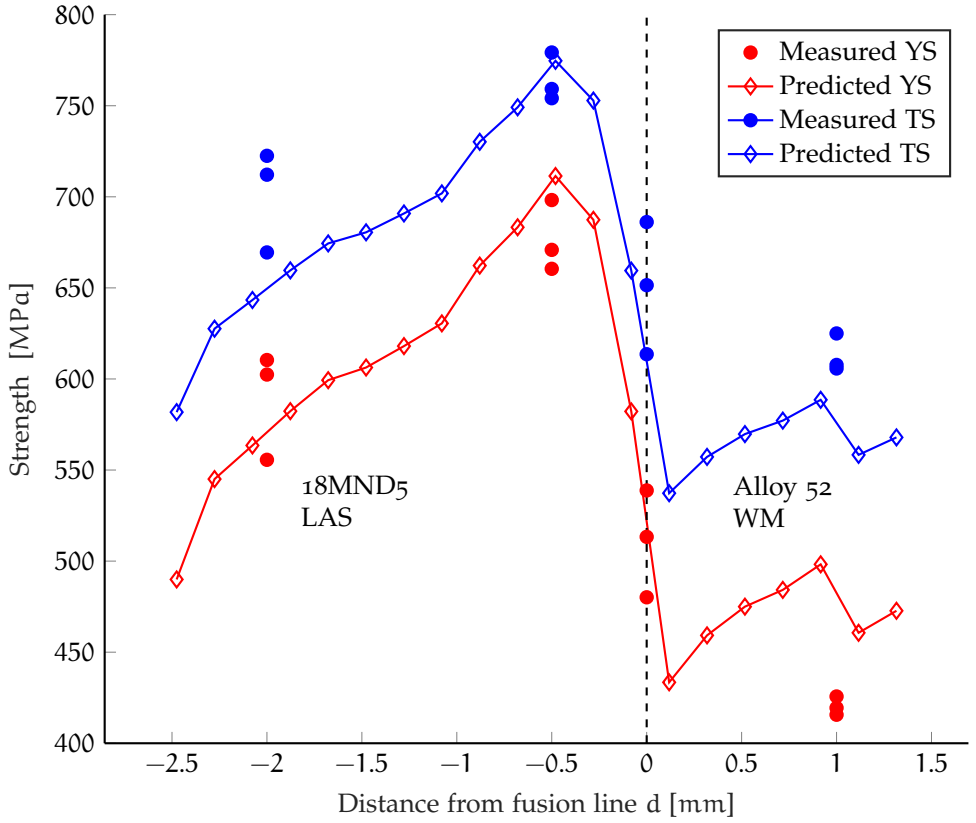

Figure 21: VTT model for hardness and strength applied to minimum hardness data. Comparable to figure 22.

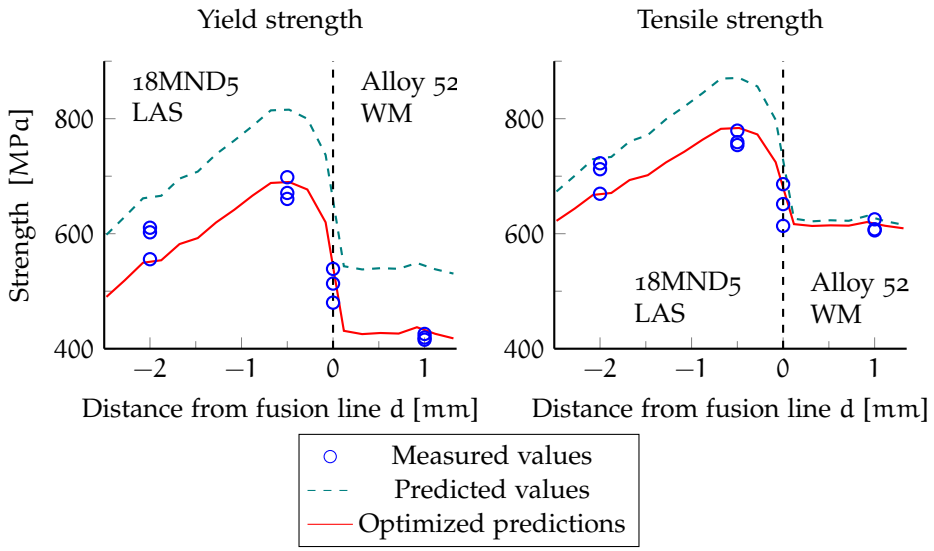

Figure 22: VTT model for hardness and strength applied to median hardness data. Tensile test results are also displayed. Negative distance is the LAS side and positive side is the stainless weld metal.

shown that the test load affects the measured hardness as a phenomenon known as the size effect. [39]

6.3 CRACK PATH AND DUCTILE FRACTURE OF AN ALLOY 52 DMW

Crack paths of MU1 specimens and corresponding tearing resistance curves are plotted in figures 23 and 24. The red lines describe the vertical distance d to the fusion line, whereas the blue ones are J values. Both are compared to the crack extension Δ. Lines with similar styles correspond with each other.

The results agree with previous observations: if the pre-crack tip is close enough to the fusion line, it propagates towards it. The closer the pre-crack tip is to the fusion line, the lower is the tearing resistance curve. If the distance to the fusion line is too large and the crack propagates straight, the tearing resistance is significantly higher.

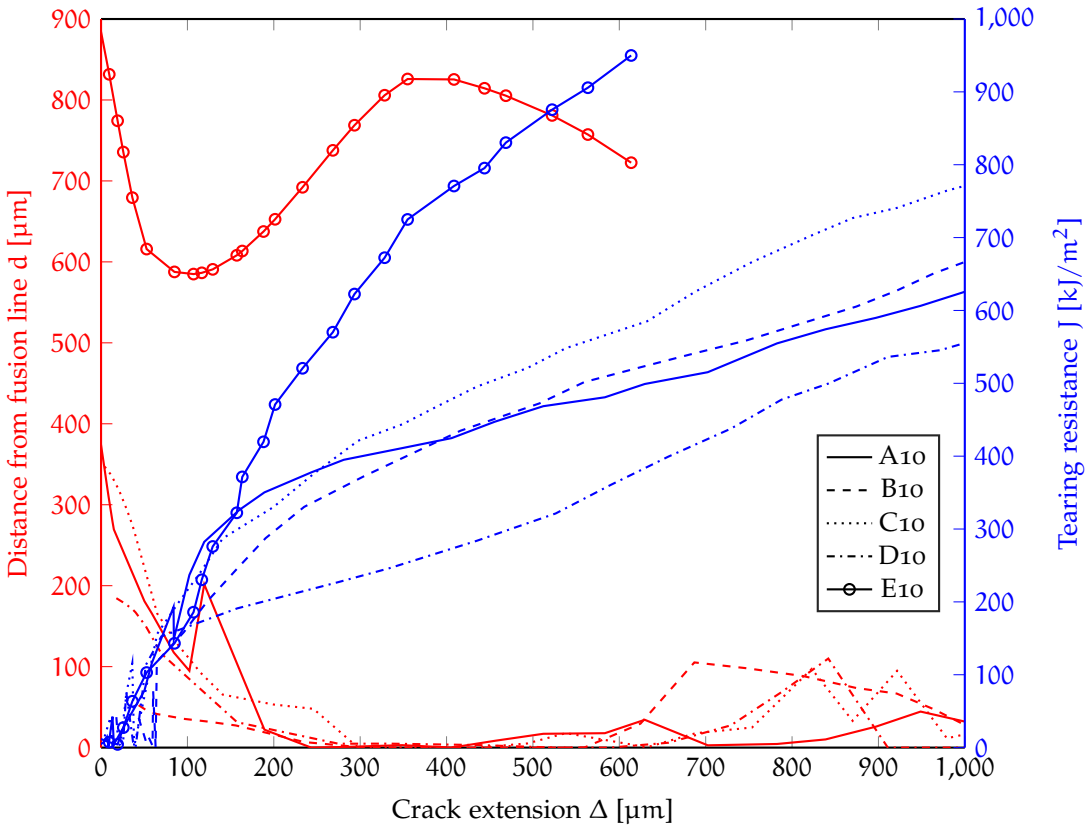

Figure 23: Tearing resistance curves and distances to fusion line for MU1 10x10 SE(B) specimens during 1mm of crack extension. Red lines depict the distance to fusion line while blue lines illustrate the corresponding tearing resistance curves.

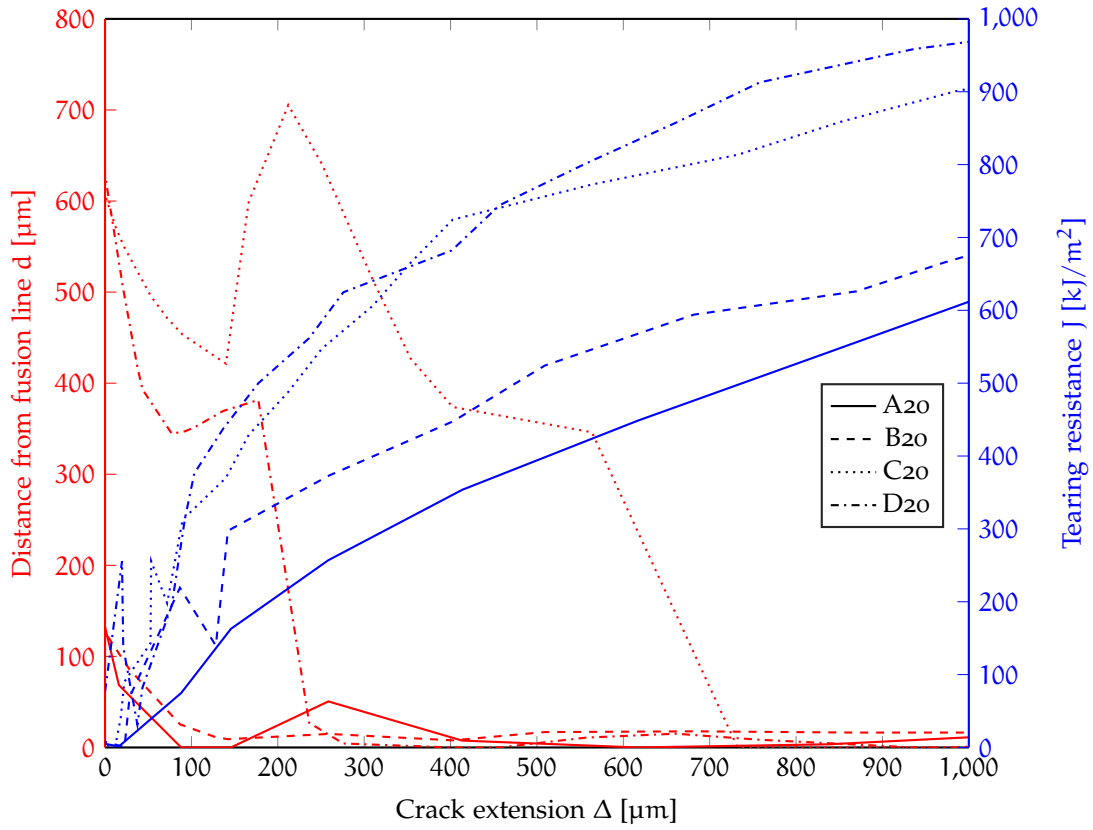

Figure 24: Tearing resistance curves and distances to fusion line for MU1 10x20 SE(B) specimens during 1mm of crack extension. Red lines depict the distance to fusion line while blue lines illustrate the corresponding tearing resistance curves.

Next, the maximum distance the cracks jumped towards the fusion line from the crack tip during the first 1mm are compared to measured J_{Ic} values. Both MU1 and NI1 distances, along with the fracture toughness results, are presented in figure 25. The method of determining the distance was similar for both, even if the data was obtained differently. Nevertheless, MU1 E10 was discarded since it did not jump to the fusion line during the first 1 mm as required. This can be seen in both figures 9 and 23.

It is evident that J_{Ic} correlates linearly with the jump. The correlation in NI1 and MU1 10x10 SE(B) sets is very clear, as indicated by linear fits. Thermal ageing duration of NI1 specimens does not, however, seem to have an impact on fracture toughness. Measured values from NI1 are comparable to the results by Kumar et al.[40]. They measured J_{Ic} values of 559 kJ/m^2 and 646 kJ/m^2 at a distance of 2 mm and 4 mm away from the FL on the LAS side as well as 671 kJ/m^2 in the LAS outside the HAZ.

Similar correlation is not clear for larger 10x20 MU1 specimens. This might be due to fluctuation of the fusion line, as can be seen in figure 26. C20 records a two

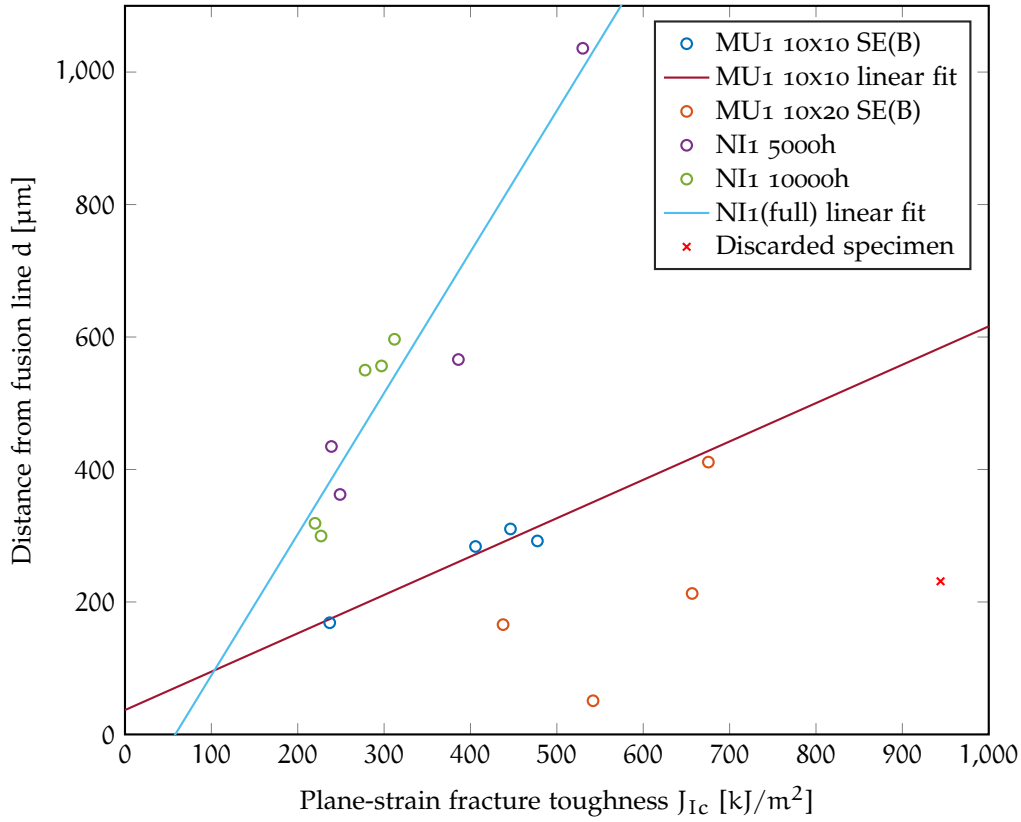

Figure 25: Ductile fracture toughness compared to maximum crack jump during the first 1mm of crack extension. Two lines are fit to illustrate correlation in respective data. Discarded specimen is MU1-E10 which never propagates to the fusion line.

times larger jump d as D20, 411 µm against 213 µm, although the distances jumped in LAS are almost the same, 285 µm and 308 µm, respectively.

The method used above to determine d does not consider such fluctuation as the NI1 data does not include explicit information about the fusion line. Consideration of a better method of analysis is left for further studies.

Comparing different sets is more challenging. MU1 and NI1 specimens were tested in different temperatures, 300 °C and 20 °C, respectively. Specimens at higher temperature record higher J_{Ic} values at same distances. The effect is inverse to Seok's findings discussed in 2.6.3 and the extent is formidable: when $d > 215\,\mu m$, J_{Ic} at 300 °C is more than two times larger than at room temperature.

MU1 and NI1 DMWs had also different LAS as base metals. This can naturally lead to different behaviours, but the difference between 18MND5 and SA508 is minimal, as can be seen from the compositions in table 2.

The different geometries might also have an effect, as explained in section 4.3.1. The 10x10 SE(B) specimens are so small that the load bearing capacity might suffer. Further studies might be needed to validate this type of analysis of J_{Ic} and d.

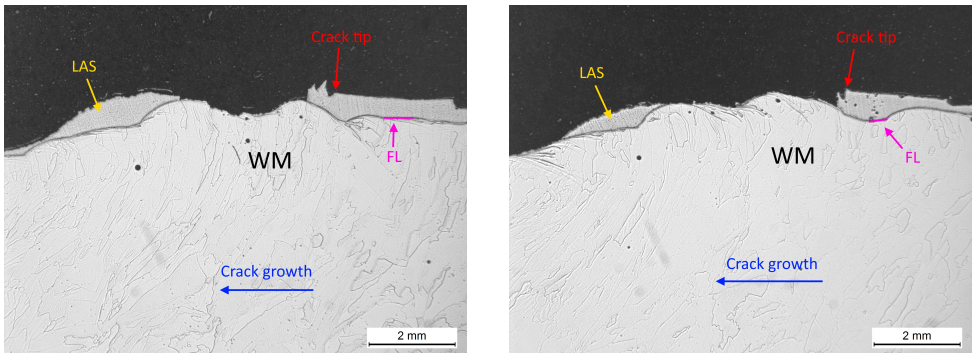

(a) C20 **(b)** D20

Figure 26: Cross-cuts of two MULTIMETAL 10x20 SE(B) specimens. Fluctuation of the fusion line is visible in both cases.

Different methods can also have an effect on the accuracy and precision on the measurements of distance to the fusion line d. NI1 profiles obtained through profilometry were averaged from three measurements whereas the cross-cuts of MU1 specimens provide only a one measurement. As discussed in section 4.3.2, it should also be noted that J_{Ic} is heavily dependent on the blunting line.

6.4 CRACK PATH AND J_C FOR AN ALLOY 52 DMW

The measured J_c values at the SA508-Alloy 52 fusion line of NI1 specimens are compared to distances between the pre-crack tip and the fusion line as measured from crack profiles. A linear fit, along with 95% confidence bounds, is calculated to illustrate and assess correlation.

The data divided into different thermal ageing durations is portrayed in figure 27. A rough correlation for all data can be seen: larger distance to fusion line indicates larger J_c values. Once divided, however, more systematic relations can be established. These relations are discussed next.

The longer the ageing time, the lower the fracture toughness J_c is for a crack initiating further from the fusion line. This is observable from slope's rise with increasing ageing time.

Even if the slope changes with ageing time, it is perhaps even more interesting that intercept does not. The line for each ageing condition finds an intercept at $J_c(d = 0) = 20.1 \pm 2.0 kJ/m^2$. Thus, the minimum fracture toughness of a specimen with a crack initiating at the fusion line does not seem to be affected by ageing.

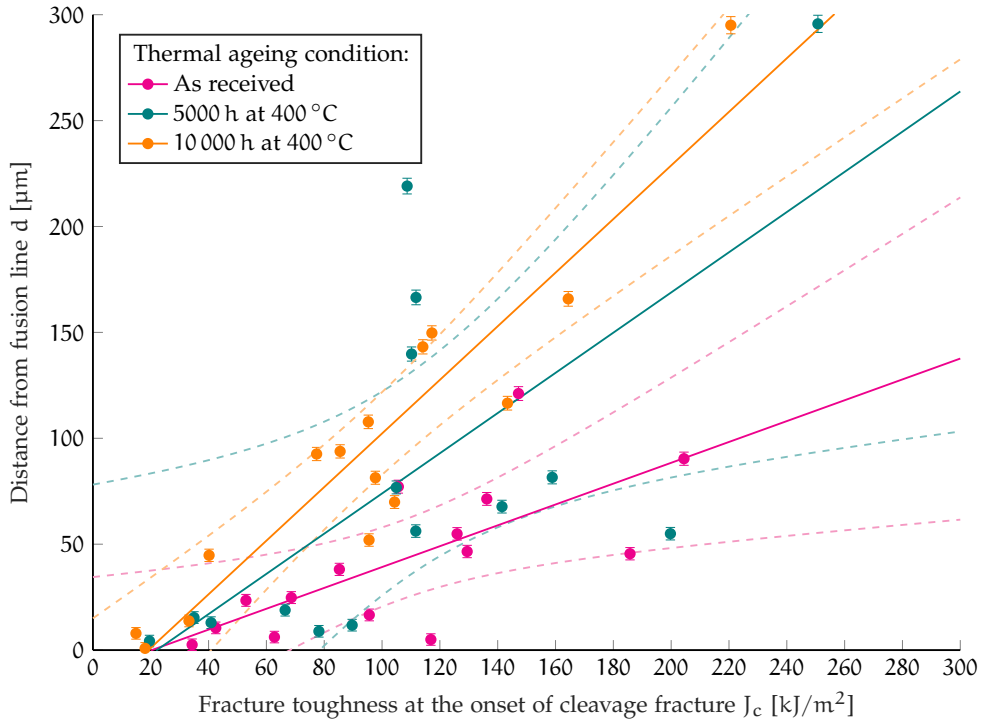

Figure 27: J_c values compared to measured jumps towards fusion line. Data from each ageing condition is marked and linearly fit separately. 95% confidence bounds for each fit are marked with dashed lines.

On the other hand, in figure 28 the data is grouped by test temperature. The fact that the linear models in figures 27 and 28 are quite similar can be expected because of the nature of the Master Curve method: as discussed in section 4.3.3, most specimens in a test series end up being tested in the same temperature once the sweet spot is determined. Therefore grouping by temperatures ends up being nearly the same as grouping by test series, which in this case are determined by ageing condition. In any case, no notable connection between test temperature and dependence of J_c on d can be identified.

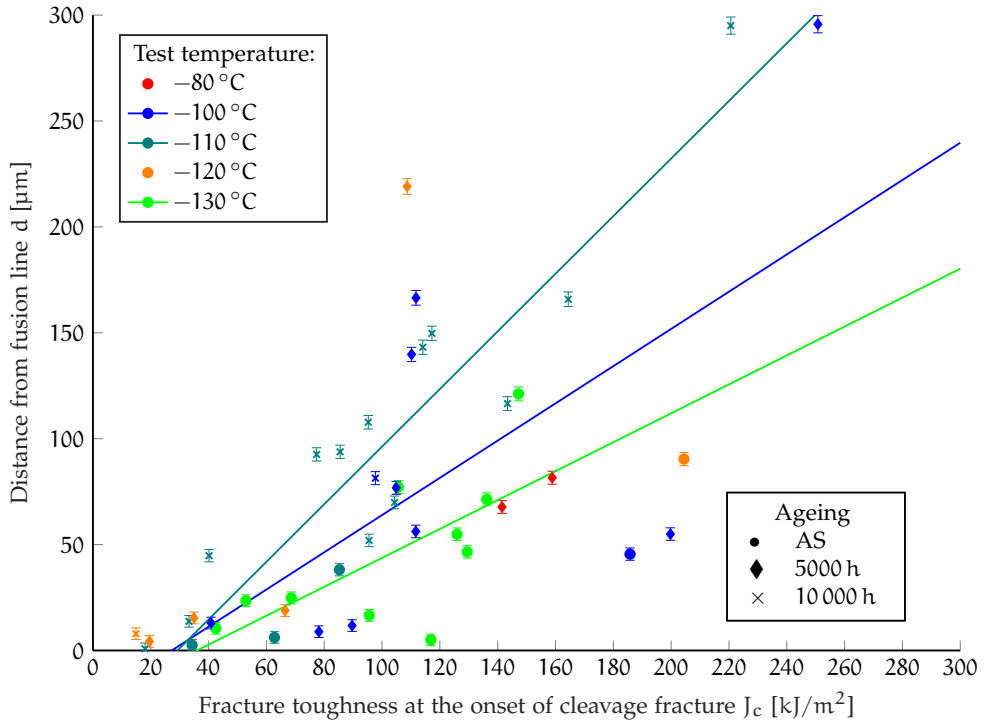

Figure 28: J_c values compared to measured jumps towards fusion line. Measurements are divided into groups according to testing temperature. Linear models are fit to groups that have enough data points. Symbol on each point denotes the ageing condition.

7 CONCLUSION

In this thesis two different, albeit very similar, Alloy 52 dissimilar metal welds (DMW) were studied from different perspectives. Research focused on the heat-affected zone (HAZ) of the low-alloy steel (LAS). This zone was identified in prior work as the region most prone to cracking.

Previous research had found out that there is a correlation between the hardness and strength for a homogeneous material. In this work, the correlation was studied around the fusion line (FL) of a DMW. A model with two parameters was used to describe the correlation. Vickers hardness measurements were bootstrapped to establish a median estimate to correlate with strength. As an alternative to the median values, an attempt was made to correlate minimum values with strength. Strength testing was performed with miniature tensile specimens.

Crack distance from the FL, d, was examined in relation to the fracture toughness of the specimen. Brittle and ductile fractures were studied independently. The specimens were of various sizes(from 5x10 to 25x50) and geometries(SE(B)or C(T)). Crack surface and d was examined from either cross-cuts or with profilometry.

The following conclusions can be made:

(i) While testing the hardness of a locally fluctuating material such as a DMW, the means of bootstrapped median values provide a viable estimate for further analyses.

(ii) A previously developed model for predicting strength from hardness(or vice versa) is viable for DMWs, but only if the parameters are modified. Possibly the model is best utilized if some tensile results verify the suitable parameters. In any case, further studies are needed.

(iii) In case of ductile fracture, if the initial crack tip is close enough to the fusion line FL, the crack deviates(jumps) there and the tearing resistance is significantly lowered.

Two different materials from different projects were studied, MU1 from MULTIMETAL and NI1 from NIWEL. A linear correlation between d and fracture toughness J_{Ic} was established. However, the slopes of linear fits for MU1

and NI1 datasets were considerably different, possibly due to differences in materials, geometries and measurement conditions as well as profiling techniques. The ageing condition of NI1 specimens did not have an effect on the correlation.

(iv) The connection between d and brittle fracture toughness J_c is also clear. In addition, ageing the material seems to reduce the tearing resistance of cracks growing further away from the fusion line. Right on the fusion line, however, where J_c is at its minimum, ageing does not seems to have an effect. Test temperature did not have a significant effect on the steepness of the J_c-d correlation.

In this work J_{Ic} was used as measure of fracture toughness at the initiation of ductile fracture. The standardized method of determining J_{Ic} depends heavily on the measured flow stress, which can fluctuate locally in the HAZ. Therefore it is debatable whether analyzing J_{Ic} is reliable for non-homogeneous materials. Fracture toughness at 1 mm crack extension, J_{1mm}, was considered as an alternative, but it could not be determined for several specimens due to insufficient crack growth for the tough materials. Anyone working with similar materials is advised to contemplate on the matter.

As an alternative for d of ductile specimens, simple vertical difference between 0 mm and 1 mm was considered. As the FL fluctuates and the ductile crack grows in a zig-zag pattern, however, the distance to the fusion line may increase during crack extension. Such increase occurs in specimen MU1-C20, as can be seen in figures 24 and 26. This increase would go unnoticed by the aforementioned vertical difference. On the other hand, it could be better to only study the final jump as it would minimize the effects of FL fluctuation and ductile zig-zag growth. Thus the best measure of a crack's slant remains an open question.

The method used to profile NI1 specimens was entirely novel. It proved practical, but an even better method for analyzing the crack profile might be in order. A non-destructive technique of profiling the crack surface as well as the fusion line from the whole thickness would be optimal. Ultrasonic testing could present an answer and is being considered at VTT. Designing such a measuring technique presents a challenge for further studies.

If the strength of a non-homogeneous material could be reliably estimated from hardness measurements, it would enable a new level of accuracy to strength as-

sessments. As numerical methods such as FEM simulations can study ever smaller specimens, they need more accurate measurements to develop their models.

If following studies confirm the correlation between tearing resistance and d presented here, the criticality of microcracks around the DMWs of structures could be assessed more accurately. Potentially, such assessments could save the operators from unnecessary maintenance without compromising safety. Further research on the topics of this work is therefore recommended.

BIBLIOGRAPHY

1. NRC. *Crack in Weld Area of Reactor Coolant System Hot Leg Piping at V. C. Summer* Information Notice 2000-17 (2000).
2. Laukkanen, A., Nevasmaa, P., Ehrnstén, U. & Rintamaa, R. Characteristics relevant to ductile failure of bimetallic welds and evaluation of transferability of fracture properties. *Nuclear Engineering and Design* **237,** 1–15. ISSN: 0029-5493 (2007).
3. Callister, W. D. J. *Materials Science and Engineering. An Introduction* 5th ed (John Wiley, New York, 1999).
4. Kamaya, M. Ramberg–Osgood type stress–strain curve estimation using yield and ultimate strengths for failure assessments. *International Journal of Pressure Vessels and Piping* **137,** 1–12. ISSN: 0308-0161 (2016).
5. Koçak, M., Webster, S., Janosch, J., Ainsworth, R. & Koers, R. *FITNET fitness-for-service(FFS) procedure* 1st. Revision MK8 (GKSS Research Center, Germany, 2008).
6. Pavlina, E. & Van Tyne, C. Correlation of Yield Strength and Tensile Strength with Hardness for Steels. *Journal of Materials Engineering and Performance* **17,** 888–893. ISSN: 1544-1024 (2008).
7. Jang, C., Lee, J., Kim, J. S. & Jin, T. E. Mechanical property variation within Inconel 82/182 dissimilar metal weld between low alloy steel and 316 stainless steel. *International Journal of Pressure Vessels and Piping* **85.** Special Issue: Advances in Structural Integrity of Nuclear Components in Asian Power Plants, 635–646. ISSN: 0308-0161 (2008).
8. Rice, J. A Path Independent Integral and the Approximate Analysis of Strain Concentration by Notches and Cracks. *Journal of Applied Mechanics* **35,** 379–386 (1968).
9. Anderson, T. L. *Fracture Mechanics. Fundamentals and Applications* 3rd ed (Taylor & Francis, Boca Raton, 2005).
10. Zhu, X. & Joyce, J. A. Review of fracture toughness (G, K, J, CTOD, CTOA) testing and standardization. *Engineering Fracture Mechanics* **85,** 1–46 (2012).

11. Wallin, K. *Fracture Toughness of Engineering Materials: Estimation and Application* 1st ed (EMAS Publishing, Warrington, 2011).

12. Wang, H., Wang, G., Xuan, F. & Tu, S. Fracture mechanism of a dissimilar metal welded joint in nuclear power plant. *Engineering Failure Analysis* **28,** 134–148. ISSN: 1350-6307 (2013).

13. Ikonen, K. & Kantola, K. *Murtumismekaniikka* 2nd, revised edition (Otatieto, Espoo, 1991).

14. Davis, J. *Tensile Testing* 2nd ed. (ASM International, Materials Park(OH, 2004).

15. Seok, C.-S. Effect of temperature on the fracture toughness of A516 Gr70 steel. *KSME International Journal* **14,** 11–18. ISSN: 1738-494X (Jan. 2000).

16. Messler, R. W. *Principles of welding: Processes, physics, chemistry, and metallurgy* 2nd ed (Wiley, New York, 2007).

17. Lindqvist, S. *Fracture mechanical characterization of multimetal welds; Multimetal hitsien murtumismekaaninen karakterisointi* en. G2 Pro gradu, diplomityö (2014-06-23), 105.

18. Huang, M. L. & Wang, L. Carbon migration in 5Cr-0.5Mo/21Cr-12Ni dissimilar metal welds. *Metallurgical and Materials Transactions A* **29,** 3037–3046. ISSN: 1543-1940 (Dec. 1998).

19. Ming, H., Zhang, Z., Wang, J., Han, E.-H. & Ke, W. Microstructural characterization of an SA508–309L/308L–316L domestic dissimilar metal welded safe-end joint. *Materials Characterization* **97,** 101–115. ISSN: 1044-5803 (2014).

20. Zerbst, U. *et al.* Review on fracture and crack propagation in weldments – A fracture mechanics perspective. *Engineering Fracture Mechanics* **132,** 200–276. ISSN: 0013-7944 (2014).

21. Mas, F. *Solidification and phase transformations in a dissimilar steel weld 18MND5/309L/308L: evolution of microstructure and mechanical properties* PhD thesis (Université de Grenoble, Dec. 2014).

22. Kou, S. *Welding Metallurgy* ISBN: 9780471434023 (Wiley-Blackwell, Hoboken, NJ, 2003).

23. Wang, H., Wang, G., Xuan, F., Liu, C. & Tu, S. Local mechanical properties of a dissimilar metal welded joint in nuclear powersystems. *Materials Science and Engineering: A* **568,** 108–117. ISSN: 0921-5093 (2013).

24. Young, G., Hackett, M., Tucker, J. & Capobianco, T. in *Comprehensive Nuclear Materials* (ed Konings, R. J.) 273–298 (Elsevier, Oxford, 2012). ISBN: 978-0-08-056033-5.

25. Hänninen, H. *et al. Dissimilar Metal Weld Joints and Their Performance in Nuclear Power Plant and Oil Refinery Conditions* VTT Tiedotteita (VTT, Espoo, Finland, 2006).

26. Hou, J. *et al.* Microstructure and mechanical property of the fusion boundary region in an Alloy 182-low alloy steel dissimilar weld joint. *Journal of Materials Science* **45,** 5332–5338. ISSN: 1573-4803 (2010).

27. Fan, K., Wang, G., Xuan, F. & Tu, S. Local failure behavior of a dissimilar metal interface region with mechanical heterogeneity. *Engineering Failure Analysis* **59,** 419–433. ISSN: 1350-6307 (2016).

28. Sarikka, T. *et al.* Effect of mechanical mismatch on fracture mechanical behavior of SA 508 – Alloy 52 narrow gap dissimilar metal weld. *International Journal of Pressure Vessels and Piping* **157,** 30–42. ISSN: 0308-0161 (2017).

29. E384-16, A. *Standard Test Method for Microindentation Hardness of Materials* West Conshohocken, PA: ASTM International, 2016.

30. E1820-13e1, A. *Standard Test Method for Measurement of Fracture Toughness* West Conshohocken, PA: ASTM International, 2013.

31. E1921-15, A. *Standard Test Method for Determination of Reference Temperature, To, for Ferritic Steels in the Transition Range* West Conshohocken, PA: ASTM International, 2015.

32. Blouin, A., Chapuliot, S. & Hamouche, W. *Evaluation of the numerical validity of the J Parameter for a crack located on a multi-material interface* English. in. **3** (2014). ISBN: 0277-027X.

33. Hariharan, P. *Basics of Interferometry* 2nd Ed. ISBN: 978-0-12-373589-8 (Academic Press, Burlington, 2007).

34. Nwaneshiudu, A. *et al.* Introduction to Confocal Microscopy. *The Journal of investigative dermatology* **132** (2012).

35. Vernon-Parry, K. Scanning electron microscopy: an introduction. *III-Vs Review* **13,** 40–44. ISSN: 0961-1290 (2000).

36. Ahonen, M. *et al. Thermal ageing and mechanical performance of narrow-gap dissimilar metal welds* English. *VTT Technology* **333.** ISBN: 978-951-38-8656-1 (VTT Technical Research Centre of Finland, Finland, 2018).

37. Oliver, W. & Pharr, G. An improved technique for determining hardness and elastic modulus using load and displacement sensing indentation experiments. *Journal of Materials Research* **7,** 1564–1583 (1992).

38. Oliver, W. & Pharr, G. Measurement of hardness and elastic modulus by instrumented indentation: Advances in understanding and refinements to methodology. *Journal of Materials Research* **19,** 3–20 (2004).

39. Mares, V., Kraus, M. & Podeprelova, A. The Effect of Applied Load on Hardness of Steels. *Materials Science Forum* **891,** 83–88 (Mar. 2017).

40. Kumar, S., Singh, P. K., Karn, K. N. & Bhasin, V. Experimental investigation of local tensile and fracture resistance behaviour of dissimilar metal weld joint: SA508 Gr.3 Cl.1 and SA312 Type 304LN. *Fatigue & Fracture of Engineering Materials & Structures* **40,** 190–206 (2016).